Magnetic Rendering: Magnetic Field Control for Haptic Display

by

Qi Zhang

Thesis submitted to the
Faculty of Graduate and Postdoctoral Studies
In partial fulfillment of the requirements
For the M.A.Sc. degree in
Electrical and Computer Engineering

School of Electrical Engineering and Computer Science
Faculty of Engineering
University of Ottawa

Abstract

As a solution to mid-air haptic actuation with strong and continuous tactile force, Magnetic Rendering is presented as an intuitive haptic display method applying an electromagnet array to produce a magnetic field in mid-air where the force field can be felt as magnetic repulsive force exerted on the hand through the attached magnet discs. The magnetic field is generated by a specifically designed electromagnet array driven by direct current. By attaching small magnet discs on the hand, the tactile sensation can be perceived by the user. This method can provide a strong tactile force on multiple points covering user's hand and avoid cumbersome attachments with wires, thus it is suitable for a co-located visual and haptic display. In my work, the detailed design of the electromagnet array for haptic rendering purposes is introduced, which is modelled and tested using Finite Element Method simulations. The model is characterized mathematically, and three methods for controlling the magnetic field are applied accordingly: direct control, system identification and adaptive control. The performance of the simulated model is evaluated in terms of magnetic field distribution, force strength, operation distance and force stiffness. The control algorithms are implemented and tested on a 3-by-3 and a 15-by-15 model, respectively. Simulations are performed on a 15-by-15 model to generate a haptic human face, which results in a smooth force field and accurate force exertion on the control points.

Acknowledgements

This thesis is based on research during my graduate studies at the Multimedia Computing Research Laboratory (MCRLab) of University of Ottawa.

Foremost, I would like to express my sincere gratitude to my supervisor, Dr. Abdulmotaleb El Saddik, for giving me the opportunity to conduct research on this rising and challenging field and guiding me forward along the innovative path.

Besides my supervisor, I would like to acknowledge my colleague Dr. Haiwei Dong for the inspiring discussions and effective collaboration.

I thank my mother, Xiaojuan Wu, who has been giving her heart-warming support all throughout my graduate studies.

Last but not the least, I would like to thank my fiance, Tianyu Su, for his love, encouragement and support.

Table of Contents

List of Tables

List of Figures

Chapter 1

Introduction

1.1 Magnetic Rendering

In pursuing realistic interactions with virtual or remote objects, the science of haptics has garnered enormous interest as the core source of realizing manual interaction with an environment.

Haptics in general refers to the touch interactions for the purpose of perceiving or manipulating the environment. During the past two decades, thrilling possibilities have opened up by introducing haptics to various disciplines involving virtual reality [1, 2], teleoperations [3], medical training [4], and many other applications, where haptic rendering [5, 6] plays a key role in generating force feedback.

In the context of human interaction with virtual objects, rendering is labelled as the process of imposing certain stimuli on the user to convey the properties of the virtual object [7]. The properties may contain detailed perceptive information ranging from shape to texture, elasticity and so on.

To explore the virtual environment, one of the most common approaches is to apply a proxy robotic device that has been adapted in many haptic devices, such as the Geomagic Touch X (formerly Sensable Phantom Desktop) by 3D Systems [8, 9]. Geomagic Touch X enables users to interact with virtual objects via a robotic pen with an articulated arm

attached. The force feedback is exerted when the proxy pen contacts a virtual object in the form of resistance for the users to perceive. A similar approach can be seen in Lorentz force magnetic levitation devices [10], in which the articulated arm is replace by magnetic force. Because this method provides point-wise force feedback, it is not intuitive in terms of human perception using hands and so is not suitable for co-located 3D visual and haptic display.

A solution to this problem is mid-air tactile sensation generation, which is addressed by wearable haptic devices [11, 12, 13, 14], air jet [15], air vortex [16, 17], ultrasound [18, 19], and magnetic force [20, 21]. Wearable haptic devices are cumbersome and need fitting to the user's hand before using. Air jet, air vortex and ultrasound are known for long operation distance but very weak force strength, and they can only generate discrete focal force points. Magnetic repelling force, on the other hand, is much stronger within short distances and can form a smooth, continuous force field in space. The idea of *Magnetic Rendering* is introduced refers to a new haptic display method that applies an electromagnet array to produce a magnetic field in the air where the force field can be felt as a magnetic repulsive force exerted on the hand through the magnet discs attached.

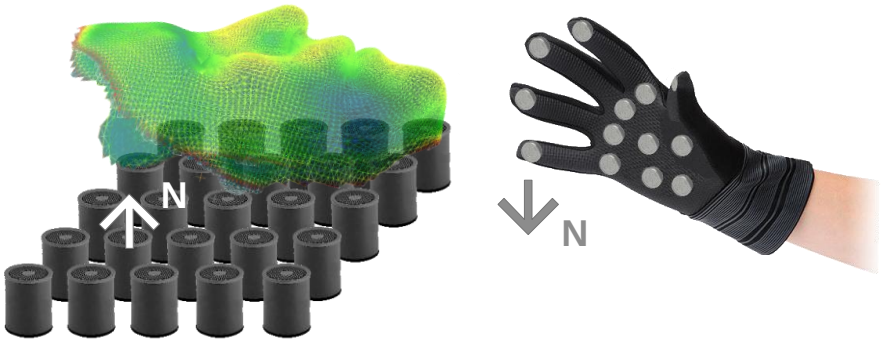

Figure 1.1: Magnetic Rendering concept.

A magnetic rendering system is presented to render volumetric shapes by applying a magnetic repelling force to produce tactile sensation in space. By attaching small magnet discs on users' hands, users can feel the haptic shapes just by moving their hands through the air. The proposed system allows users to perceive a continuous force field as shown in

Fig. 1.1. The magnetic field is generated by a carefully designed electromagnet array whose advantage is proved by Finite Element Method (FEM) simulations and can be controlled directly or by using the system identification and adaptive filter approach.

1.2 Contribution

The main contributions of this work are the following:

- A magnetic rendering system is proposed for users to feel volumetric shapes with little attachments on their hands by using magnetic repelling force as the tactile feedback approach.
- A new electromagnet array is designed to produce high magnetic field strength outside one side of the array, which is then evaluated by FEM simulations. For a single electromagnet model, the design of a magnetic concentrator lifts its magnetic field up and the mechanics behind which is derived mathematically. The introduction of a magnetic isolator shields the magnetic field between every two of the elements and avoids severe interference. The final configuration of an array is optimized design in terms of magnetic field interference and smoothness of the force field.
- The linearity characteristics of the system are proved and based on which three control methods– direct control, system identification, and adaptive control– are applied to the electromagnet array to generate the desired magnetic field for users to perceive.

1.3 Thesis Organization

The remainder of this thesis is organized as follow:

- Chapter 2 discusses the existing work related to applying magnetic force as an approach of contactless tactile sensation generation. The related work of the main-

stream methods for producing mid-air force feedback are discussed and compared, through which the advantages of using magnetic force are revealed.

- Chapter 3 introduces the basic knowledge of magnetic field analysis theories and the concept of Halbach array, which is an example of manipulating the magnetic field by a special arrangement of magnets. Furthermore, multi-input-multi-output system identification and recursive least squares algorithm for adaptive control are introduced, which are referred to in Chapter 4 where the control methods for our system are developed.

- Chapter 4 describes the design of the electromagnet array and the algorithms for controlling the magnetic field. First a single electromagnet model is designed which can concentrate the magnetic field to the upper surface, and then the configuration of an array of electromagnets is optimized. The characteristics of the model are analysed, based on which, three methods for controlling the magnetic field are developed.

- Chapter 5 presents the performance of the designed model and the control methods by finite element simulation. The simulation methodology is followed by the performance analysis of a single designed electromagnet model and a 3-by-3 electromagnet array. A final set of simulation is done on a 15-by-15 electromagnet array which aims to produce the shape of a human face in mid-air.

- Chapter 6 presents the conclusion of this work and several feasible ideas related to future work.

Chapter 2

Related Work

2.1 Contactless Tactile Sensation Generation

A variety of methods have been studied to create contactless tactile sensation; however, no device can render a continuous volumetric shape with strong force feedback for users to perceive. One of the most popular methods uses wearable devices that aims to attach force vector stimulators directly on the users' hands and impose feedback such as vibration [11, 12] and cutaneous forces [13, 14]. These methods all suffer from the fact that the attachments can be cumbersome and cannot produce actual pressure on the skin, making them unsuitable for haptic volumetric shape-rendering purposes. Air jet was chosen intuitively in [15] to produce contactless haptic feedback with low accuracy. Unlike standard jets of air, air vortices (rings of air) are also used in devices such as AirWave [17] and AIREAL [16]. However, both of these methods have low fidelity due to the non-focusing stimulation area. Ultrasound radiation force is another candidate applied [18, 19] to generate discrete focal force points in 3D space. The drawback of this method is that the ultrasound acoustic force is very weak, and only limited focal points can be generated.

Magnetic force is widely used in magnetic levitation because it is sufficient to counteract gravity or other imposed force. In recent years, it has been adopted by a number of devices [20, 21] as a mid-air force feedback actuation method. Although the high strength of magnetic force is a desired property in haptic rendering applications, it still has drawbacks.

For example, the force between magnets decreases rapidly with the distance, and it is hard to control due to its non-linear nature.

Magnetic force is adopted as the mid-air tactile feedback in this design due to its strength and contactless nature. The short operation distance problem is addressed by a new design of electromagnet array, which proves to have near-linear characteristics that facilitate the control method design.

2.2 Magnetic Force for Contactless Haptic Interaction

Magnetic force between two magnets obeys the complex electromagnetism rules. When one of them is an electromagnet, the exerted force can be controlled by the amount of electric current running in the winding and is much stronger compared to the pressure of the air vortex or ultrasound acoustic force. Another merit of magnetic force is that it can form continuous force volume in nature compared with other methods that can only produce discrete force points. The limitation of using magnetic force for haptic rendering is that it cannot render sharp shapes due to the fact that the magnetic field is oval-shaped in nature.

For electromagnets used for haptic force actuation purposes, ferrite cores are desired because they have high magnetic permeability that can help generate a strong magnetic field; however, their use results in non-linearity of the produced force in respect to the stimulating current [22]. Moreover, the produced magnetic force is highly non-linear with the distance between the magnets; in fact, magnetic force drops with cube of the distance between the magnets. When it comes to an array of electromagnets, the superposition of the magnetic field renders controlling the coils individually nearly impossible. All these properties make precise control a challenging task.

FingerFlux [20] is a haptic device that generates near-surface force feedback for tabletops using attractive and repulsive magnetic force and vibration to guide the users when

approaching the screen. An array of electromagnets is applied as force feedback actuators, and magnets are attached on users' hands as force receivers. However, because the device is not specifically designed for haptic volume shape display, the force produced is not strong enough for this design, and because there is no numerical analysis of the force generated by the array, no control method can be derived.

Co-located 3D graphic and haptic display [21] is another device using force between electromagnet arrays and magnets for haptic rendering. For the force receiver, a pen with magnets attached is designed for a user to hold so that the force feedback can be felt. The limitation of this method is that the force feedback is single-point; that is, users can only feel the force on one point at a certain time.

For haptic rendering purposes, the force feedback not only needs to be strong enough for the user to perceive from a distance, but it also needs to cover several parts of the user's hand simultaneously for the user to feel multiple force points at the same time.

The electromagnet array model in this design is optimized in terms of layout and space between every two elements. Besides that, the physical characteristics of the force generated are determined in order to derive a control method.

2.3 Electromagnet Array Design and Control

Electromagnet arrays are mostly used for the purpose of magnetic levitation as planer motors [23, 24]; however, some ideas involving boosting the magnetic field strength can be tapped out to work for haptic rendering.

To augment the magnetic field above the electromagnet, one can increase the number of turns of the coil or raise the stimulating current value so that the spread magnetic field is increased by boosting the total magnetic field. The current running in the wires has a strict restraint due to material and manufacturing limitations such as the current capacity of the wire and the heating effect of the coil. Moreover, small electromagnets are desired so that the force field generated can be felt with detail, which renders a large number of wire turns impossible. Therefore, the main consideration is concentrating the magnetic

field to only one pole of the electromagnet, which can also increase the efficiency of energy usage. Ideally, the model is expected to be unipolar. However, because unipolar magnets do not exist in reality, one can only augment the magnetic field on one side by arranging permanent magnets in special patterns.

One good example is the Halbach array [25], which aligns permanent magnets in a special way so that the magnetic field is reinforced on one side and cancelled on the other side to near zero. The Halbach effect is discovered in one-dimensional arrays and is extended to two-dimensional arrays [26] where the one-side magnetic field is nearly obtained by the special arrangements. However, on the side in which the magnetic field is strengthened, the direction of the field is interchanging, which is undesirable for haptic rendering where only one pole is needed.

In this design of electromagnets suitable for haptic rendering, we develop a new model with a magnetic field concentrator inspired by the Halbach effect, which proves to have very good performance.

Chapter 3

Background

3.1 Magnetic Field Analysis Theory in the Study of Magnetostatics

3.1.1 General Maxwell's Field Equations

The fundamental theory for electromagnetic analysis is Maxwell's equation group, which is written in the vectorial form as follows [22].

$$\nabla \times \mathbf{H} = \mathbf{J} + \frac{\partial \mathbf{D}}{\partial t} \tag{3.1a}$$

$$\nabla \times \mathbf{E} = -\frac{\partial \mathbf{B}}{\partial t} \tag{3.1b}$$

$$\nabla \cdot \mathbf{B} = 0 \tag{3.1c}$$

$$\nabla \cdot \mathbf{D} = \rho_{\mathrm{e}} \tag{3.1d}$$

In this equation group, the symbols stand for the following:

H, magnetic field intensity [$\mathrm{A\,m^{-1}}$];

B, magnetic flux density [T];

$\mathbf{D}$, electric flux density [$\mathrm{C\,m^{-2}}$];

$\mathbf{E}$, electric field intensity [$\mathrm{V\,m^{-1}}$];

$\mathbf{J}$, free current density [$\mathrm{A\,m^{-2}}$];

ρ_e, volume density of free electric charges [$\mathrm{C\,m^{-3}}$];

∇, nabla operator, which defines curl operation.

These equations are also known as the laws of Ampere-Maxwell 3.1a, Faraday 3.1b, Gauss-Faraday 3.1c, and Gauss 3.1d.

Notice that $\mathbf{J}$ and ρ_e in the previous equations can be viewed as the source of the electromagnetic field, which have the relationships known as the current conservation equation,

$$\nabla \cdot \mathbf{J} + \frac{\partial \rho_\mathrm{e}}{\partial t} = 0, \tag{3.2}$$

with the assumption that at each point in a space, the field vector and all its derivatives are continuous.

To make a general solution possible, three more equations are required, which are the Ohm's law

$$\mathbf{J} = \sigma \mathbf{E} \tag{3.3}$$

and the relations

$$\mathbf{B} = \mu \mathbf{H} \tag{3.4}$$

$$\mathbf{D} = \varepsilon \mathbf{E} \tag{3.5}$$

where σ is the electric conductivity [$\Omega^{-1}\,\mathrm{m^{-1}}$], and

$$\mu = \mu_0 \mu_\mathrm{R} \tag{3.6}$$

is the magnetic permeability with $\mu_0 = 4\pi 10^{-7}$ [$\mathrm{H\,m^{-1}}$]. It is the measure of the ability of a material to conduct the magnetic field formations within itself. Materials with high permeabilities allow magnetic field lines to get through more easily than others. Materials with

high permeabilities include iron and the other ferromagnetic materials. Other materials, such as plastics, wood, and air, have much lower permeabilities around 0. Moreover,

$$\varepsilon = \varepsilon_0 \varepsilon_\mathrm{R} \tag{3.7}$$

is the permittivity with $\varepsilon_0 = 8.854^{-12}[\mathrm{F\,m^{-1}}]$. These parameters describe characteristics of the medium, which, in most cases, are functions of various other parameters such as temperature. Thus the problem becomes rather cumbersome, although it can be simplified by approximations under certain conditions.

3.1.2 Magnetostatics

Magnetostatics is a short name for static magnetic fields, where the current is considered as static, so there is no time dependence. The Ampere's law is simply

$$\nabla \times \mathbf{H} = \mathbf{J}, \tag{3.8}$$

and Eq. 3.2 becomes

$$\nabla \cdot \mathbf{J} = 0, \tag{3.9}$$

which describes that without charge accumulation $\frac{\partial \rho_\mathrm{e}}{\partial t}$, all current lines either close on themselves or extend to infinity.

3.1.3 Magnetization

The magnetic properties of a medium can be described with magnetization vector

$$\mathbf{M} = \mathbf{B}/\mu_0 - \mathbf{H}, \tag{3.10}$$

which can be rewritten as the constitutive relationship

$$\mathbf{B} = \mu_0(\mathbf{H} + \mathbf{M}), \tag{3.11}$$

Magnetization can only exist in a medium and vanishes in free space where Eq. 3.4 holds.

Eq. 3.11 shows that when present in an electromagnetic field, the internal source of currents appears in the material in the form of volume and surface magnetization current [27]

$$\mathbf{J}_{\mathrm{VM}} = \nabla \times \mathbf{M} \tag{3.12}$$

$$\mathbf{J}_{\mathrm{SM}} = \mathbf{M} \times \vec{n} \tag{3.13}$$

where $\mathbf{J}_{\mathrm{VM}}$ is the volume magnetization current, and $\mathbf{J}_{\mathrm{SM}}$ is the surface magnetization current. $\mathbf{M}$ is the magnetization vector field, and $\vec{n}$ denotes the unit normal vector to the surface of the magnet.

3.1.4 Magnetic Force Calculation

In the case of magnets imposing force on each other, magnetic force imposed on a magnet due to a non-uniform magnetic field can be calculated as

$$\mathbf{F} = \int_{\Omega} \mathbf{M}_{\mathrm{magnet}} \cdot \nabla \mathbf{B} dV \tag{3.14}$$

where Ω represents the volume of the magnet, and $\mathbf{M}_{\mathrm{magnet}}$ is the magnetization of the magnet [28].

3.1.5 Magnetic Potential

To solve Eq. 3.8, it is often convenient to introduce the vector potential $\mathbf{A}$ defined by

$$\mathbf{B} = \nabla \times \mathbf{A} \tag{3.15}$$

such that in the case of magnetostatics, Eq. 3.1c becomes

$$\nabla \cdot \mathbf{A} = 0, \tag{3.16}$$

and the magnetic field is found through

$$\mu\mathbf{H} = \nabla \times \mathbf{A}. \tag{3.17}$$

Thus, in the stationary case, the potential $\mathbf{A}$ is

$$(\nabla \cdot \nabla)\mathbf{A} = -\mu\mathbf{J}. \tag{3.18}$$

3.2 Halbach Array

3.2.1 Halbach Effect

For applications that focus on maximizing the magnetic flux on only one side of the magnet array, arrangements of the array with the capability to augment the magnetic field on one side are highly preferred.

One simple example is the refrigerator magnet, in which the magnetic field seems to only exist on one side. This application originated from a theory called the Halbach effect [25], which has proved mathematically that a magnet whose magnetic flux only exists on one side can be constructed.

Arrangements of magnet arrays taking advantage of the Halbach effect prove to have significantly increased magnetic flux compared with that of individual magnet components of the array.

3.2.2 One-Dimensional Halbach Array

The arrangement of a one-dimensional Halbach array has a rotating pattern that can be extended to any length is shown in Fig. 3.1.

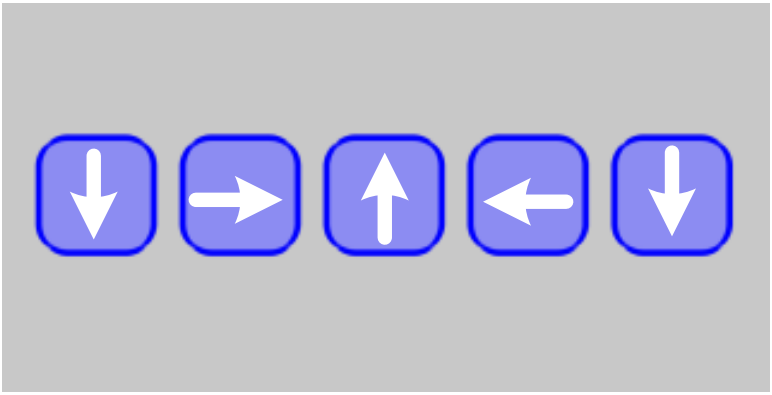

Figure 3.1: Arrangement of a one-dimensial Halbach array

The arrows in Fig. 3.1 indicate the magnetization directions of the permanent magnets, and the corresponding magnetic field distribution is shown in Fig. 3.2.

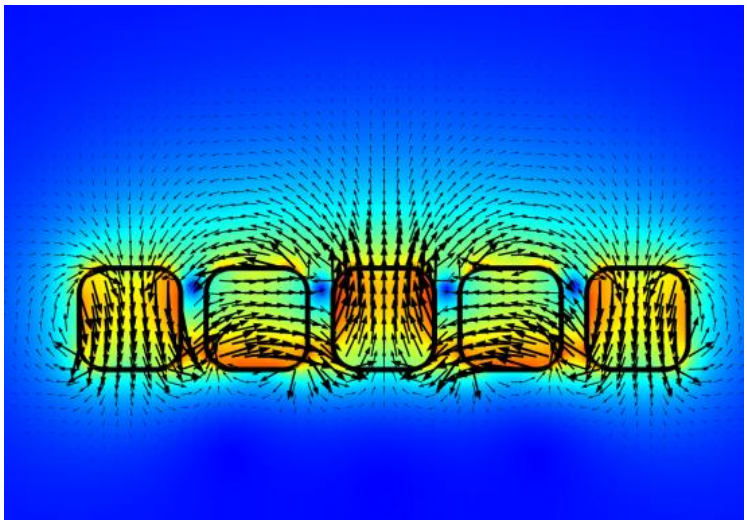

Figure 3.2: Magnetic field of a one-dimensial Halbach array

As shown in Fig. 3.2, the magnetic field is augmented on the top side and reduced on the bottom.

3.2.3 Two-Dimensional Halbach Array

The design of a two-dimensional Halbach array [26] is introduced in the patent of magnetic arrays with increased magnetic flux, which is depicted in Fig. 3.3.

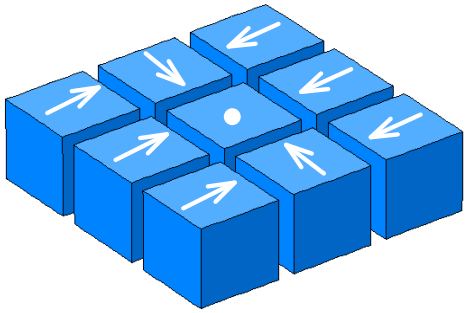

Figure 3.3: Arrangement of a two-dimensial Halbach array

This arrangement enables a magnetic field to be increased only on the upper side of the array.

3.3 Multi-Input, Multi-Output Linear System Identification

3.3.1 Identification by Regression

Regression analysis is a classic statistical tool [29] that is widely adopted in system engineering where its applications to multi-variable identification [30, 31, 32] are well accepted. Both linear and non-linear processes can be identified by techniques based on least-squares regression procedures, which greatly facilitate identification when using several simultaneous inputs.

If identification of m coefficients is required in each of n simultaneous linear transformations of the form

$$x_{\mathrm{j}} = a_{0\mathrm{j}} + a_{1\mathrm{j}}u_1 + a_{2\mathrm{j}}u_2 + \cdots + a_{\mathrm{mj}}u_{\mathrm{m}}, \tag{3.19}$$

where $u_{\mathrm{i}}(i = 1, 2, \ldots m)$ are the m simultaneous inputs, $x_{\mathrm{j}}(j = 1, 2, \ldots n)$ are the corresponding n outputs, and a_{ij} are the coefficients need to be identified. If the same $u_{\mathrm{i}}(i = 1, 2, \ldots m)$ appear in all n equations, all $a_{\mathrm{ij}} \forall i, j$ may be identified over more than m measurement instances. Therefore, all the coefficients of the above n equations may be identified simultaneously.

3.3.2 Derivation of the Regression Parameters

The derivation of the regression parameters is shown in the case of the single-output static problem depicted in Fig. 3.4.

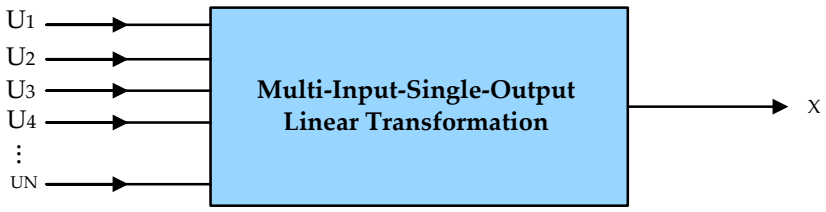

Figure 3.4: Multi-input, single-output (MISO) system identification

The system can be described by Eq. 3.20.

$$X = a_0 + a_1U_1 + a_2U_2 + \cdots + a_{\mathrm{m}}U_{\mathrm{m}} \tag{3.20}$$

Assume r sets of measurements of X and U_{j} $(j = 0, 1, 2, \ldots m)$ are taken. a_{j} can be derived by the following procedure: First, the r sets of measurements are stored. Second, these r sets of measurement are used to calculate $\overline{X}$ and $\overline{U}$, with $\overline{X}$ being the average of X, and $\overline{U}$ being the average of U over the above r sets of measurement. Then we define

$$\begin{aligned} x &\triangleq X - \overline{X}, \\ u &\triangleq U - \overline{U}, \end{aligned} \tag{3.21}$$

Eq. 3.20 becomes

$$x = a_1 u_1 + a_2 u_2 + \cdots + a_{\mathrm{m}} u_{\mathrm{m}} \tag{3.22}$$

or, in vector form,

$$x = \mathbf{u}^T \mathbf{a} \tag{3.23}$$

where $\mathbf{u}$, $\mathbf{a}$ are both column vectors with length m. Consequently, the r sets of measurement satisfy

$$\begin{aligned} x_{(1)} &= \mathbf{u}_{(1)}^T \mathbf{a} \\ x_{(2)} &= \mathbf{u}_{(2)}^T \mathbf{a} \\ \cdots &\quad \cdots \\ x_{(\mathrm{l})} &= \mathbf{u}_{(\mathrm{l})}^T \mathbf{a} \\ \cdots &\quad \cdots \\ x_{(\mathrm{r})} &= \mathbf{u}_{(\mathrm{r})}^T \mathbf{a} \end{aligned} \tag{3.24}$$

where (l) indicates the lth set of measurement. We further define a vector $\boldsymbol{\chi}$ and a matrix $\mathbf{U}$ as follows:

$$\boldsymbol{\chi} \triangleq [x_{(1)} \ldots x_{(\mathrm{l})} \ldots x_{(\mathrm{r})}]^T \tag{3.25}$$

$$\mathbf{U} \triangleq \begin{bmatrix} \mathbf{u}_{(1)}^T \\ \mathbf{u}_{(2)}^T \\ \vdots \\ \mathbf{u}_{(\mathrm{r})}^T \end{bmatrix} = \begin{bmatrix} u_{1(1)} & \ldots & u_{\mathrm{j}(1)} & \ldots & u_{\mathrm{m}(1)} \\ \vdots & & \vdots & & \vdots \\ u_{1(\mathrm{l})} & \ldots & u_{\mathrm{j}(\mathrm{l})} & \ldots & u_{\mathrm{m}(\mathrm{l})} \\ \vdots & & \vdots & & \vdots \\ u_{1(\mathrm{r})} & \ldots & u_{\mathrm{j}(\mathrm{r})} & \ldots & u_{\mathrm{m}(\mathrm{r})} \end{bmatrix} \tag{3.26}$$

Hence, Eq. 3.24 can be rewritten as

$$\boldsymbol{\chi} = \mathbf{U} \cdot \mathbf{a}. \tag{3.27}$$

Then estimated coefficients $\hat{\mathbf{a}}$ yield estimation of $\boldsymbol{\chi}$ as

$$\hat{\boldsymbol{\chi}} = \mathbf{U} \cdot \hat{\mathbf{a}}. \tag{3.28}$$

To obtain the best estimated coefficients in a least-squares sense, the goal is to minimize the squared errors of the estimation defined in Eq. 3.29,

$$\boldsymbol{S} \triangleq (\boldsymbol{\chi} - \mathbf{U}\hat{\mathbf{a}})^{\boldsymbol{T}}(\boldsymbol{\chi} - \mathbf{U}\hat{\mathbf{a}}) = \boldsymbol{tr}[(\boldsymbol{\chi} - \mathbf{U}\hat{\mathbf{a}})(\boldsymbol{\chi} - \mathbf{U}\hat{\mathbf{a}})^{\boldsymbol{T}}] \tag{3.29}$$

where $tr\ldots$ is the trace of the matrix inside [33]. To minimize the expression in Eq. 3.29, the following equation has to be satisfied:

$$\frac{\partial S}{\partial \hat{a}_{\mathrm{i}}} = 0, \quad \forall i \in [1, m]. \tag{3.30}$$

This can be written in vector form as

$$\frac{\partial S}{\partial \hat{\mathbf{a}}} = \frac{\partial tr[(\boldsymbol{\chi} - \mathbf{U}\hat{\mathbf{a}})(\boldsymbol{\chi} - \mathbf{U}\hat{\mathbf{a}})^T]}{\partial \hat{\mathbf{a}}} = 0. \tag{3.31}$$

According to the calculation rules of the trace function, Eq. 3.31 becomes

$$\begin{aligned} \frac{\partial S}{\partial \hat{\mathbf{a}}} &= \frac{\partial tr[(\boldsymbol{\chi} - \mathbf{U}\hat{\mathbf{a}})(\boldsymbol{\chi} - \mathbf{U}\hat{\mathbf{a}})^T]}{\partial \hat{\mathbf{a}}} \\ &= 2(\mathbf{U}^T\mathbf{U}\hat{\mathbf{a}} - \mathbf{U}^T\boldsymbol{\chi}) = 0, \end{aligned} \tag{3.32}$$

which results in

$$\mathbf{U}^{\boldsymbol{T}}\mathbf{U}\hat{\mathbf{a}} = \mathbf{U}^{\boldsymbol{T}}\boldsymbol{\chi}. \tag{3.33}$$

Thus, the best estimate $\hat{\mathbf{a}}$ for $\mathbf{a}$ in a least-squares sense is

$$\hat{\mathbf{a}}^T \triangleq \begin{bmatrix} \hat{a_1} & \hat{a_2} & \dots & \hat{a_{\mathrm{m}}} \end{bmatrix}^T = (\mathbf{U}^T\mathbf{U})^{-1} \cdot \mathbf{U}^T\boldsymbol{\chi}. \tag{3.34}$$

Note that $\mathbf{U}^T\mathbf{U}^{-1}$ exists only if $\mathbf{U}$ has full column rank.

3.4 Adaptive Filter and Recursive Least-Squares Algorithm

Adaptive filters can be used to estimate the coefficients of an unknown linear system, which require little computational storage and eliminate the matrix inversion problem [34, 35, 36]. The block diagram of an adaptive filter is shown in Fig. 3.5.

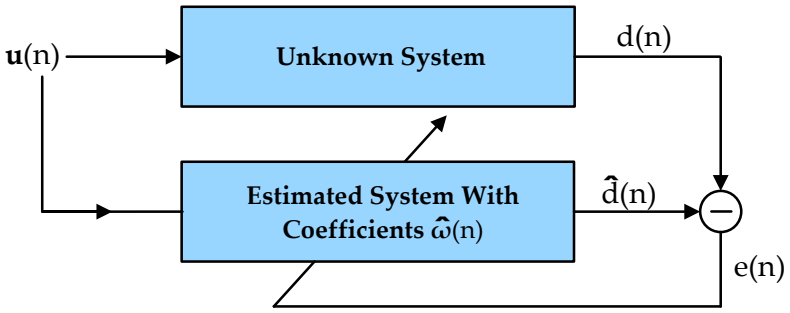

Figure 3.5: Block diagram of an adaptive filter

In this equation, $\mathbf{u}(n) = [u_1(n), u_1(n) \dots u_{\mathrm{k}}(n)]$ is the input vector at instant n, and $d(n)$ is the output. $e(n) = d(n) - \hat{d(n)}$ is the *a posteriori* output error, and $\hat{\boldsymbol{\omega}}(n) = [\hat{\omega}_1(n), \hat{\omega}_2(n) \dots \hat{\omega}_{\mathrm{k}}(n)]$ is the estimated coefficient vector at instant n.

Algorithms such as least mean squares (LMS) [37], normalized least mean squares (NLMS), and recursive least squares (RLS) [38] can be applied as update rules of the filter, among which RLS algorithm is known for its fast convergence.

The estimated output at instant n is

$$\hat{d}(n) = \hat{\omega}_1(n)u_1(n) + \hat{\omega}_2(n)u_2(n) + \cdots + \hat{\omega}_{\mathrm{k}}(n)u_{\mathrm{k}}(n). \tag{3.35}$$

The RLS algorithm aims to update the coefficients $\hat{\boldsymbol{\omega}}$ that reduces the weighted least-squares error function in Eq. 3.36

$$C(\hat{\boldsymbol{\omega}}(n)) = \sum_{i=1}^{n} \lambda^{n-i} e^2(i) \tag{3.36}$$

where λ is called the forgetting factor within the range of $[0, 1]$ because the effect of the error in the past is decreasingly significant.

According to Wiener-Hopf equations [39], the cost function in Eq. 3.36 is minimized when

$$\frac{\partial C(\hat{\boldsymbol{\omega}}(n))}{\partial \hat{\boldsymbol{\omega}}(n)} = -2 \sum_{i=1}^{n} \lambda^{n-i} \mathbf{u}(i)[d(i) - \mathbf{u}^T(i)\hat{\boldsymbol{\omega}}(n)] = 0, \tag{3.37}$$

which results in

$$\begin{aligned} \hat{\boldsymbol{\omega}}(n) &= \left[\sum_{i=1}^{n} \lambda^{n-i} \mathbf{u}(i)\mathbf{u}^T(i) \right]^{-1} \sum_{i=1}^{n} \lambda^{n-i} \mathbf{u}(i) d(i) \\ &= \mathbf{R}^{-1}(n)\mathbf{p}(n) \end{aligned} \tag{3.38}$$

where $\mathbf{R}(n)$ is the deterministic correlation matrix of the input, and the $\mathbf{p}(n)$ is the deterministic cross-correlation vector between the input and desired output.

The matrix inversion if avoided in the RLS algorithm by the use of the matrix inversion lemma [40], based on which $\mathbf{R}^{-1}(n)$ can be calculated as

$$\mathbf{R}^{-1}(n) = \frac{1}{\lambda} \left[\mathbf{R}^{-1}(n-1) - \frac{\mathbf{R}^{-1}(n-1)\mathbf{u}(n)\mathbf{u}^T(n)\mathbf{R}^{-1}(n-1)}{\lambda \mathbf{u}^T(n)\mathbf{R}^{-1}(n-1)\mathbf{u}(n)} \right]. \tag{3.39}$$

Chapter 4

Proposed Method

4.1 Magnetic Rendering System

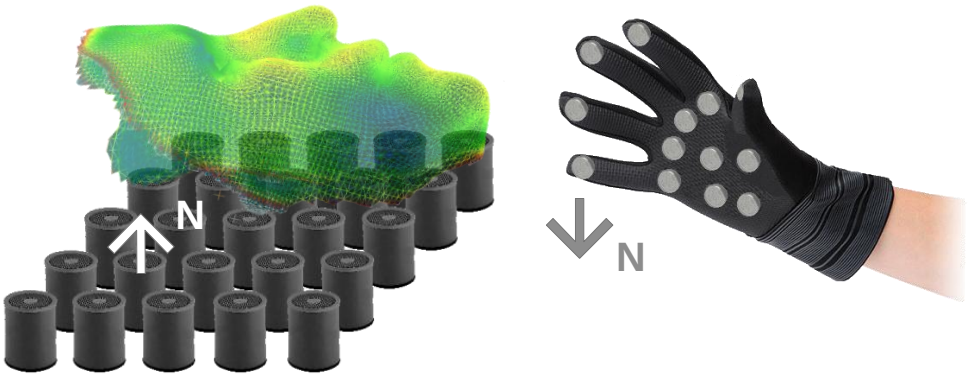

Figure 4.1: Magnetic force feedback

The proposed magnetic rendering system's haptic interface applies repulsive magnetic force as haptic feedback to render desired shapes haptically in mid-air for users to perceive. The haptic shape is rendered by a specially designed electromagnet array for the purpose of providing the corresponding haptic feedback. Because magnetic repulsive force can only be exerted on like poles facing each other, an opposite magnetization is required on the hand. An easy way to do this is to attach one or several small disc-shaped permanent

magnets to the user's hand or onto a glove, as shown in Fig. 4.1.

The size of the electromagnet array can be scaled as needed, and each of the electromagnets is driven by direct current (DC) output from power sources. For a given set of 3D volumetric data, preprocessing is required to fit the data with the size and the force range of the electromagnet array, after which the data is fed into the controller and transformed into suitable current values based on the control algorithm. The final configuration of current values is then imposed on the array to generate the magnetic field. When placing hands with magnets attached above the array, the pressure sensation of the virtual object can be perceived in mid-air.

The architecture of the proposed magnetic rendering system is shown in Fig. 4.2.

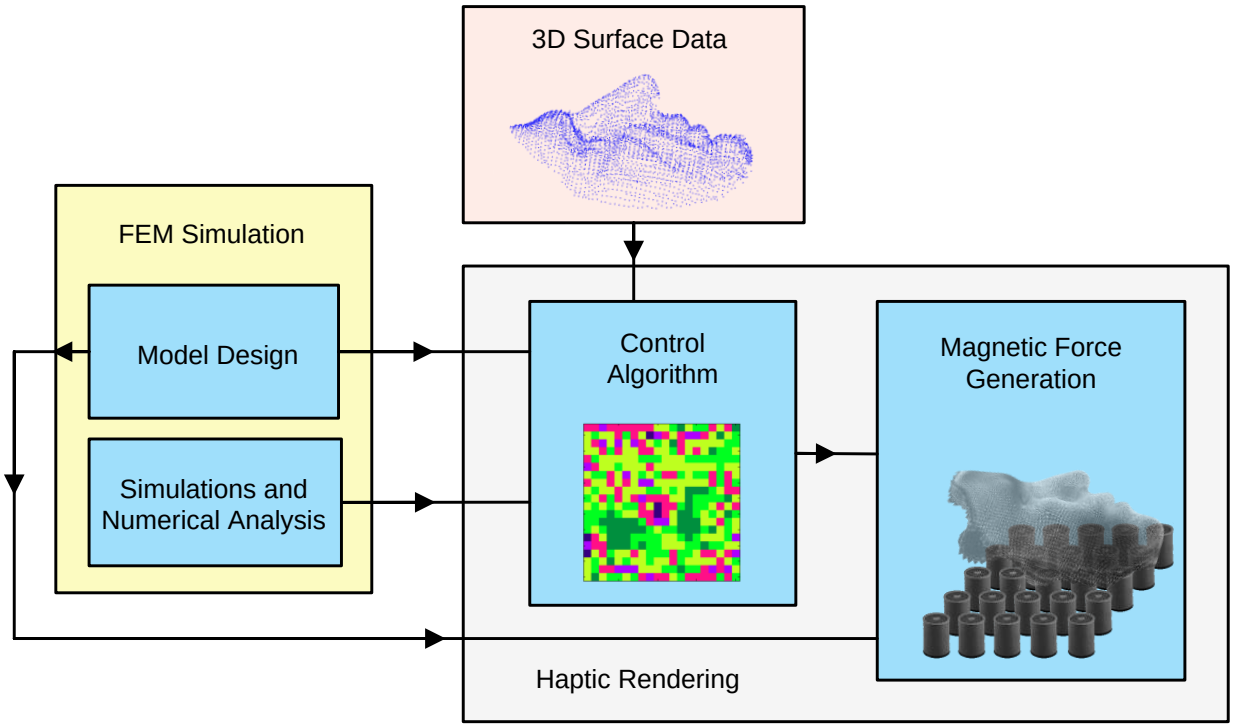

Figure 4.2: Magnetic Rendering System

The magnetic rendering system is mainly composed of three parts:

- *FEM simulation*, which is used for designing the electromagnet array model, and is responsible for analysing various electromagnetic properties of the model.

- *3D surface data*, which can be obtained from 3D scanners or other volumetric data-generation tools.

- *Haptic rendering*, which produces a magnetic force against the user magnets under the control of a designed algorithm based on the properties of the model and the simulation results.

Having the system structure determined, our main task breaks down into two parts: electromagnet array actuator design and control methods development.

In this section, the design concerns and methods of the entire electromagnet array are introduced. The control methods based on the properties of the actuator model are introduced in Section 4.3.

4.2 Design of the Electromagnet Array

4.2.1 Concerns of the Design

When designing an electromagnet array model suitable for haptic rendering, the main concerns fall into three categories:

- *Actuation*, which is the strength of the repulsive force exerted between electromagnets and the permanent magnets on the user's hand

- *Controllability*, which refers to the controllable range and accuracy of the force produced by the electromagnet array

- *Feasibility*, which includes manufacturing realities that constrain the choice of parameters in design

Strong actuation force is certainly a desirable outcome, which guides the design in many aspects such as the geometry, material and dimensions of a single electromagnet model. The degree to which the magnetic force can be controlled depends mainly on the isolation

of the field generated by each electromagnet against others. The nature of magnetic field superposition cannot be avoided, but it can be reduced by magnetic shielding. On the other hand, in order to form a smooth force field, the superposition property can be taken advantage of by choosing proper material and adjusting the dimension when configuring the array. All design attempts and parameter sets have to be reasonable in terms of manufacturing limitations, and products in the market must be consulted as references.

For the criteria of design, the force generated is the most important criterion for a haptic device when making decisions, besides which the magnetic flux density and its norm serve as indicators of the magnetic field distribution. In the simulation step, magnetic flux density B is solved by FEM simulation based on the magnetostatic model. For the evaluation and control of magnetic repulsive force, the vertical force F_{z} is considered the object. The expression for the vertical magnetic force is derived from Eq. 3.14 as

$$\begin{aligned} F_{\mathrm{z}} &= \int_{\Omega} M_{\mathrm{disc}} \cdot \nabla \mathbf{B}(\vec{r}, \vec{\theta}, \vec{z}) dV \\ &= \int_{\Omega} M_{\mathrm{disc}} \cdot \left(\frac{\partial}{\partial r} + \frac{\partial}{\partial \theta} + \frac{\partial}{\partial z} \right) \mathbf{B}(\vec{r}, \vec{\theta}, \vec{z}) dV \\ &= \int_{\Omega} M_{\mathrm{disc}} \cdot \frac{\partial B_{\mathrm{z}}}{\partial z} \vec{z} dV \end{aligned} \tag{4.1}$$

where M_{disc} is the magnetization of the magnet disc, which is along the z direction with Ω as its volume.

For the following discussions, two sets of coordinates are used for the overall array and individual element respectively as shown in Fig. 4.3.

The Cartesian coordinates $(\vec{x}, \vec{y}, \vec{z})$ are used for describing the locations of the elements in the array, and the cylindrical coordinates $(\vec{r}, \vec{\theta}, \vec{z})$ are used for magnetic field derivations for the individual electromagnets.

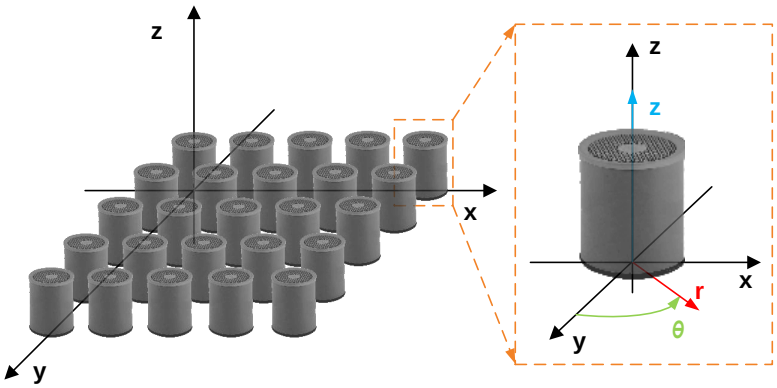

Figure 4.3: Global Cartesian coordinates and local cylindrical coordinates

4.2.2 Structure of the Electromagnet

The evolution of the designed magnetic field concentrated electromagnet model is depicted in Fig. 4.4.

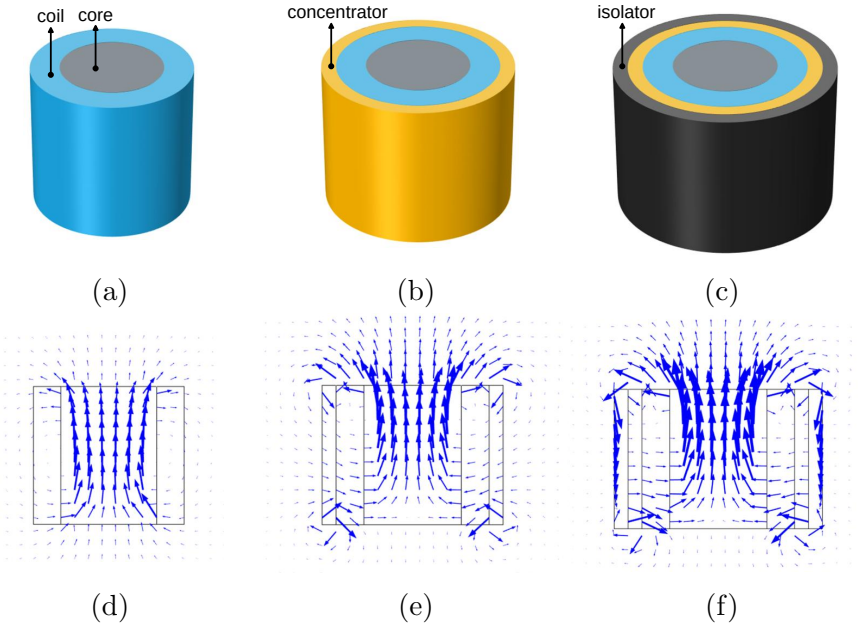

Figure 4.4: Structure and magnetic field distribution of the three models

We start with a traditional electromagnet model shown in Fig. 4.4a, which only consists of a metal core and coil whose magnetic field is uniformly distributed as in Fig. 4.4d when DC is imposed. To augment the power usage efficiency, the magnetic field needs to be concentrated to the upper part of the model, thus a magnetic field concentrator is

introduced as shown in Fig. 4.4b with the concentrating effect depicted in Fig. 4.4e. When constructing an array, the model is expected to be isolated so that the magnetic field generated by neighbouring elements will not cause serious interference. To realize this, an isolator is designed to shield the magnetic field, and its effect can be seen in Fig. 4.4f.

When stimulated by DC, a magnetic field is exerted by the inner coil due to Ampere's law and is magnified by the soft iron core in the centre. The permanent magnet ring functions as a magnetic field concentrator, and the Mu-metal shell serves as an isolator. These two layers grant the model sound properties regarding magnetic field strength, concentration, and isolation. A summary of the structure of the model is shown in Fig. 4.5, and the corresponding designed parameters are listed in Table 4.1.

Table 4.1: Summary of Design Parameters

Components	Material	Dimension	Key Physics Properties
Core	Soft iron	Height: 2cm Diameter: 1.4cm	HB curve
Coil	Copper	Height: 2cm Thickness: 0.4cm Turns: 1000	Current capacity: $[-1\text{A}, 1\text{A}]$
Concentrator	Iron	Height: 2cm Thickness: 0.2cm	Magnetization: $5 \times 10^5 \text{A/m}$ Direction: $-\vec{r}$
Shell	Mu-metal	Height: 2cm Thickness: 0.2cm	Relative permeability: $80,000$

The detailed design of this structure and the reason for choosing the corresponding dimensions and other parameters of the model are discussed in the following sections in the following order:

- Section 4.2.3, design of the inner coil
- Section 4.2.4, design of the magneic field concentrator and the physics mechanics behind it
- Section 4.2.5, design of the Mu-metal isolator and how decisions are made about the shape of the shell

- Section 4.2.6, layout of the electromagnet array and how the distance between each two elements is chosen

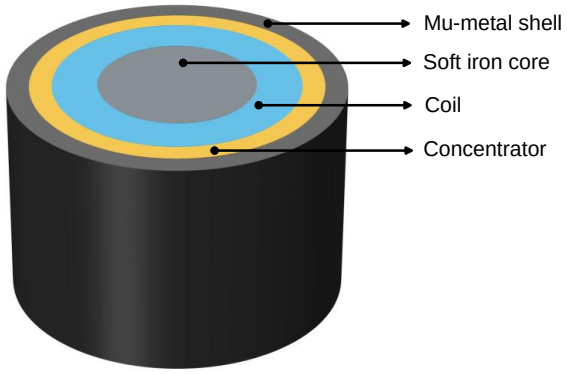

Figure 4.5: Designed electromagnet structure

4.2.3 Configurations of the Inner Coil

The parameters of the inner coil are chosen based on industrial standards and manufacturing limits. The dimensions of the coil are set based on a coil-winding manufacturer [41], where the height of the coil is set as 2cm, and the inner and outer diameters are set as 1.4cm and 2.2cm respectively. This means the cylinder core of the coil has a height of 2cm and a diameter of 1.4cm, and the windings have a total cross-sectional area of $2\times0.4 = 0.8\text{cm}^2$. To generate a powerful magnetic field, the number of turns is set as 1000, thus the cross-sectional area for the wire is set to be 0.08mm^2, which is very close to gauge 28 of the standard wire sizes according to the American Society for Testing and Materials (ASTM) Standard B258-02 [42] whose current carrying capacity is about -1A. Therefore, the current range of the electromagnet is from -1A to 1A.

The core of the coil is designed to be made of soft iron, whose carbon content is very low and thus has a relatively soft texture compared to hard iron. Soft iron can withstand a strong magnetic field while not reaching the saturation point, hence is a preferred material as electromagnetic core. However, soft iron is a non-linear magnetic

material, whose permeability is not a constant but depends on the magnetic field strength. The B-H curve of soft iron is depicted in Figure 4.6.

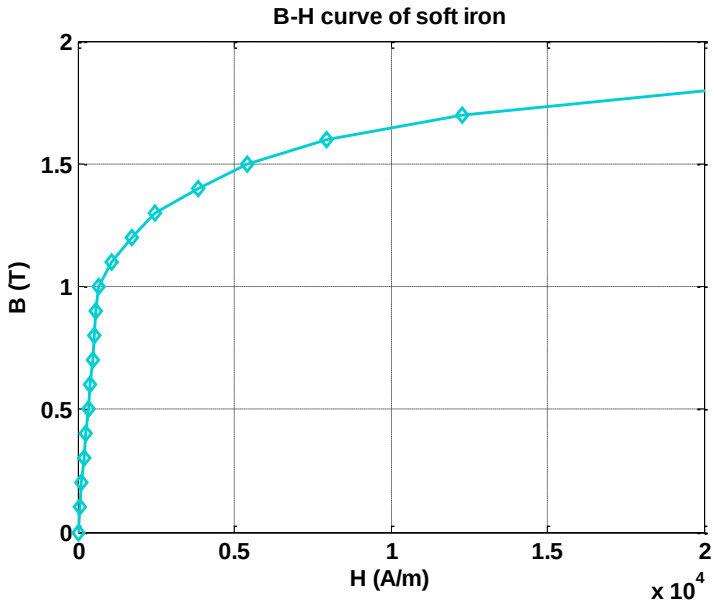

Figure 4.6: B-H curve of soft iron

4.2.4 Magnetic Field Concentration

To augment the magnetic field above one pole of the electromagnet, the number of turns of the coil can be increased or the stimulating current value can be raised so that the spread magnetic field is increased by boosting the total magnetic field. The current running in the wires has a strict restraint due to material and manufacturing limitations such as the current capacity of the wire and the heating effect of the coil. Moreover, small-sized electromagnets are desired so that the force field generated can be felt with detail, which renders a large number of wire turns impossible. Therefore, the main consideration is concentrating the magnetic field to only the north pole of the electromagnet, which can also increase the efficiency of energy usage. As stated previously, ideally the model is expected to be unipolar. However, because unipolar magnets do not exist in reality, the magnetic field can only be augmented on one side by arranging permanent magnets in special patterns. Two good examples are the Halbach array [25] and the magnetic arrays

with increased magnetic flux [26], which are introduced in Chapter 3, section 3.2.

Inspired by this theory, the coil is encased in a cylinder ring permanent magnet as a method to enhance the magnetic flux on the upward side. The directions of magnetization and corresponding current flow are depicted in Fig. 4.7.

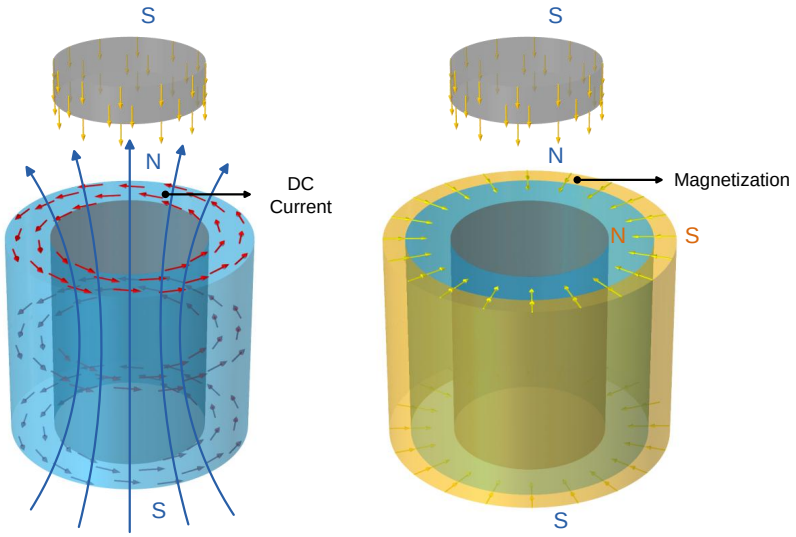

Figure 4.7: Current and magnetization directions

By imposing counterclockwise current into the coil in the vertical view, the magnetic field lines generated are pointing upward according to the right-hand rule, thus the coil can be viewed as a magnet with the north pole on the top. The permanent ring, the concentrator, is then radially magnetized with north the pole pointing to the axis.

The concentrator works by contributing the current density as the magnetization current flowing both within the volume and on the surface of the concentrator. From Eq. 3.12 and Eq. 3.13 introduced in Chapter 3, section 3.1.3, the detailed equations in our case are

$$\mathbf{J}_{\mathrm{VM}} = \nabla \times \mathbf{M}(\vec{r}, \vec{\theta}, \vec{z}) \tag{4.2}$$

$$\mathbf{J}_{\mathrm{SM}} = \mathbf{M}(\vec{r}, \vec{\theta}, \vec{z}) \times \vec{n} \tag{4.3}$$

where $\mathbf{J}_{\mathrm{VM}}$ is the volume magnetization current, and $\mathbf{J}_{\mathrm{SM}}$ is the surface magnetization

current. $\mathbf{M}(\vec{r},\vec{\theta},\vec{z})$ is the magnetization vector field expressed in a cylindrical coordinates system, and $\vec{n}$ denotes the unit normal vector to the surface of the concentrator. $\nabla \times \mathbf{M}(\vec{r},\vec{\theta},\vec{z})$ is the curl of the vector field, which can be written explicitly in a cylindrical coordinate system as

$$\nabla \times \mathbf{M}(\vec{r},\vec{\theta},\vec{z}) = \frac{1}{r}(\frac{\partial M_z}{\partial \theta} - \frac{\partial M_\theta}{\partial z})\vec{r} + (\frac{\partial M_r}{\partial z} - \frac{\partial M_z}{\partial r})\vec{\theta} + \frac{1}{r}(\frac{\partial (rM_\theta)}{\partial r} - \frac{\partial M_r}{\partial \theta})\vec{z}. \tag{4.4}$$

Here in this design, the magnetization direction is along $-\vec{r}$ only with magnitude M_r; i.e. the magnetization vector field is

$$\mathbf{M}(\vec{r},\vec{\theta},\vec{z}) = -M_{\mathrm{r}}\vec{r}. \tag{4.5}$$

The volume magnetization current expressions of the radial magnetization can be obtained by substituting Eq. 4.5 into Eq. 4.2:

$$\begin{aligned} \mathbf{J}_{\mathrm{VM}} &= \nabla \times (-M_{\mathrm{r}}\vec{r}) \\ &= \vec{0}(\mathrm{A/m^2}) \end{aligned} \tag{4.6}$$

For the surface magnetization current, the calculation is done by applying Eq. 4.3 to the top, bottom, inner side, and outer side surface of the concentrator, respectively.

$$\begin{aligned} \mathbf{J}_{\mathrm{SM}}^{\mathrm{top}} &= (-M_{\mathrm{r}}\vec{r}) \times \vec{z} \\ &= M_{\mathrm{r}}\vec{\theta}(\mathrm{A/m}) \end{aligned} \tag{4.7}$$

$$\begin{aligned} \mathbf{J}_{\mathrm{SM}}^{\mathrm{bottom}} &= (-M_{\mathrm{r}}\vec{r}) \times (-\vec{z}) \\ &= -M_{\mathrm{r}}\vec{\theta}(\mathrm{A/m}) \end{aligned} \tag{4.8}$$

$$\begin{aligned}\mathbf{J}_{\mathrm{SM}}^{\mathrm{inner-side}} &= (-M_{\mathrm{r}}\vec{r}) \times (-\vec{r}) \\ &= \vec{0}(\mathrm{A/m})\end{aligned} \tag{4.9}$$

$$\begin{aligned}\mathbf{J}_{\mathrm{SM}}^{\mathrm{outer-side}} &= (-M_{\mathrm{r}}\vec{r}) \times \vec{r} \\ &= \vec{0}(\mathrm{A/m})\end{aligned} \tag{4.10}$$

From Eq. 4.7, it can be seen that the concentrator contributes to the top surface current with a counterclockwise magnetization current and to the bottom surface current with a clockwise magnetization current according to Eq. 4.8. Moreover, no volume current is generated, which can be seen from Eq. 4.9 and Eq. 4.10. The equivalent surface current generated by the concentrator is shown in Fig. 4.8.

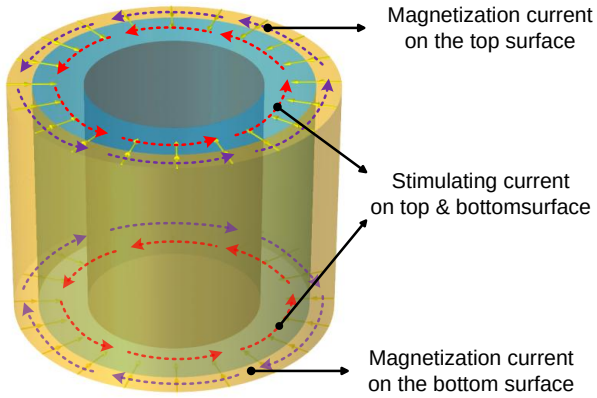

Figure 4.8: Surface magnetization current of the concentrator

It can be seen from the figure that the directions of the magnetization current and the current in the coil are the same on the top surface of the concentrator but are the opposite on the bottom surface. Thus, the magnetic field is augmented on the top and reduced on the bottom.

In reality, the magnetization value of a normal bar magnet can be 10^5A/m, whereas

for iron it can be as large as 10^6A/m. To ensure that the electromagnet model and the magnet discs have magnetic field strength of approximately the same orders of magnitude, the magnetization of the concentrator is set as 5×10^5A/m and that of the disc magnets is 10^6A/m.

4.2.5 Magnetic Shielding

For magnetic field isolation purposes, alloys with high permeabilities ($\mu_r \gg 1$) are suitable to be used as shells outside the electromagnet. The shield acts as a better conductor of magnetic flux and thus provides a lower reluctance path than air or other materials of the electromagnet. The magnetic field lines, which would have appeared at the radius of the electromagnet, will then stay within the shell.

Mu-metal is one of the most efficient materials for magnetic field shielding. It is a nickel-iron alloy composed of about 80% nickel and other materials, including iron, copper, and so on, depending on the mix. The relative permeability of Mu-metal can reach as high as $80,000 - 100,000$ compared with several thousand for steel and 1 for air. The thickness of the Mu-metal shell is set as 2mm, which is one of the Mu-metal sheet product specifications [43]. Part of the cross section along the length of the electromagnet is depicted in Figure 4.9 to show the effect of magnetic field shielding.

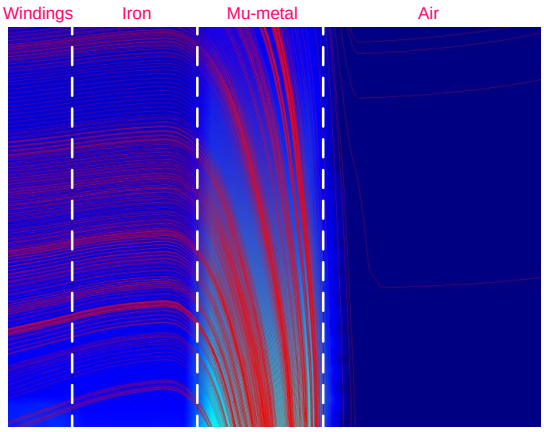

Figure 4.9: Magnetic field shielding

It can be seen from Figure 4.9 that most of the magnetic field lines are retained in

the Mu-metal shell; therefore, the magnetic field flux spreading into the air is reduced substantially.

For the shape of the Mu-metal shell, the original idea is to make it a half-open cylindrical chamber closed only at one end while leaving the desired magnetic pole exposed. The purpose of this plan is first to shield the radial magnetic field and, second, to shield one pole of the model to make it an unipolar electromagnet. However, this idea is in conflict with the physics fact that magnetic monopoles do not exist, so simulations are run to check the feasibility of this plan.

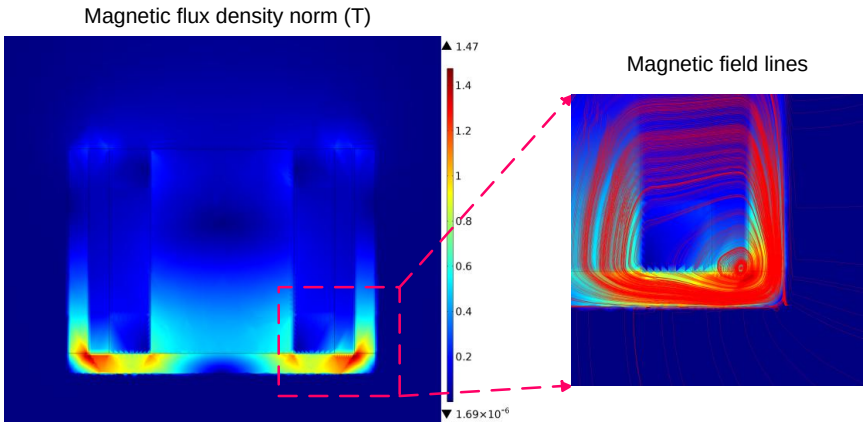

Figure 4.10: Magnetic field in the shell with bottom

The magnetic flux density norm of the electromagnet cross-section plane is depicted as an indication of magnetic field lines distribution.

As shown in Figure 4.10, although the magnetic field is shielded effectively by adding the Mu-metal shield with bottom to the model, most of the electromagnetic energy is wasted in the bottom of the shell. This is due to the fact that the magnetic field lines have to form closed loops. Because the path where the magnetic field lines meet out of the shell is blocked, they close within the shell instead, hence only a minor part of the magnetic field lines generated is ejected from the top. Therefore, the Mu-metal shell is designed to be an open-ended cylinder wrapping the concentrated model without a bottom cap. The magnetic flux density norm distribution and the values measured from 1cm above the top of the electromagnet along the axis are shown in Figure 4.11.

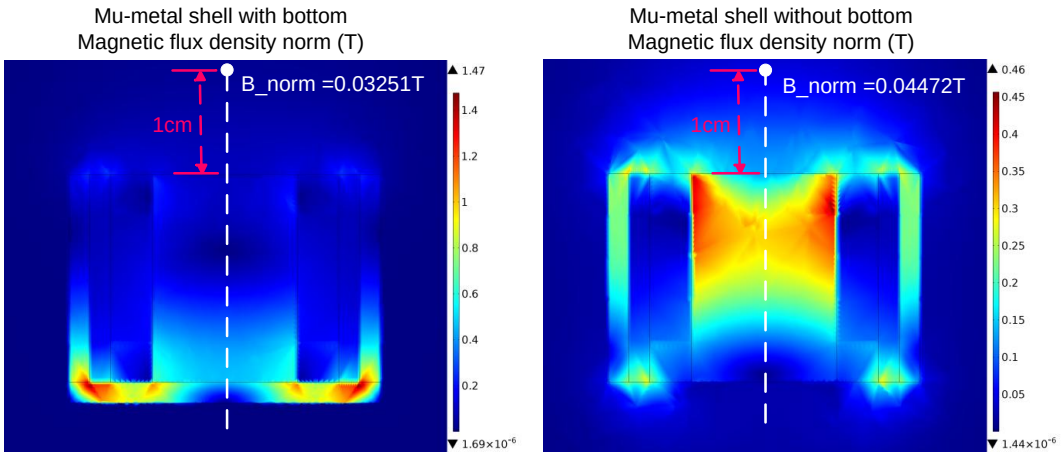

Figure 4.11: Comparison of magnetic field in two shell shapes

The magnetic field lines in the modified design concentrate mainly at the upper part of the core, which results in a stronger magnetic field above the electromagnet. Here the measurement is taken at 1cm above along the axis and shows an increase of 37.56% in the magnetic flux density norm.

4.2.6 Layout of the Electromagnet Array

To form an array using the electromagnet designed as a haptic display, the preferred arrangement of the electromagnets is compact, yet the magnetic field superposition is not so serious that the force field loses its details.

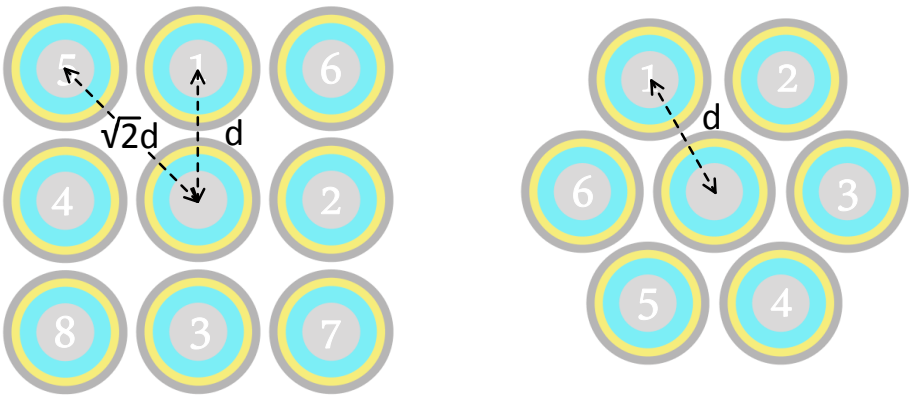

Figure 4.12: Two candidate layouts of electromagnet array

Two candidate arrangements of array have been considered, as shown in Fig. 4.12. The magnetic field interference is used here as a criterion. When considering the influence of surrounding elements to the one in the center, it can be shown that it is smaller in the square layout. By assuming the distance between the nearest two elements in both layouts is d as shown in Fig. 4.12, the magnetic field above the central element of the square layout by each of the eight surrounding elements is denoted as $B_{\mathrm{i}}^{\mathrm{square}}$ $(i = 1, 2, 3...8)$, and the hexagon layout is denoted as $B_{\mathrm{j}}^{\mathrm{hexagon}}$ $(j = 1, 2, 3...6)$. Because the magnetic field obeys the superposition principle and decays with the cube of the distance, the magnetic field above the centre generated by the surrounding elements in both layouts is calculated in Eq. 4.11:

$$\begin{aligned} B_{\mathrm{surrounding}}^{\mathrm{square}} &= \sum_{i=1}^{8} B_{\mathrm{i}}^{\mathrm{square}} \\ &= \frac{1}{d^3} \sum_{i=1}^{4} B_{\mathrm{i}}^{\mathrm{square}} + \frac{1}{(\sqrt{2}d)^3} \sum_{j=5}^{8} B_{\mathrm{j}}^{\mathrm{square}} \\ B_{\mathrm{surrounding}}^{\mathrm{hexagon}} &= \sum_{j=1}^{6} B_{\mathrm{j}}^{\mathrm{hexagon}} \\ &= \frac{6}{d^3} \sum_{j=1}^{6} B_{\mathrm{j}}^{\mathrm{hexagon}} \end{aligned} \tag{4.11}$$

In this equation, $B_{\mathrm{surrounding}}^{\mathrm{square}}$ is the magnetic field above the centre element generated by the surrounding elements in the square layout, and $B_{\mathrm{surrounding}}^{\mathrm{hexagon}}$ is that in the hexagon layout. By assuming the currents running in all the elements are of the same value, the magnetic field generated will be the same, which is denoted as B_{s}, and $B_{\mathrm{i}}^{\mathrm{square}} = B_{\mathrm{j}}^{\mathrm{hexagon}} = B_{\mathrm{s}}$, $(i = 1, 2...8,\ \ j = 1, 2...6)$. Then from Eq. 4.11, it can be seen that the calculated interference from the surrounding elements is about $\frac{5.14}{d^3} B_{\mathrm{s}}$ in the square arrangement, which is less than $\frac{6}{d^3} B_{\mathrm{s}}$ of the hexagon layout; therefore, square layout is chosen in this design.

With the layout of the electromagnet array determined, the distance between each element is another parameter of concern because it is a trade-off factor between force field smoothness and controllability. As mentioned before, the superposition effect abates the precision of control while helping to form a smooth force field for haptic perception.

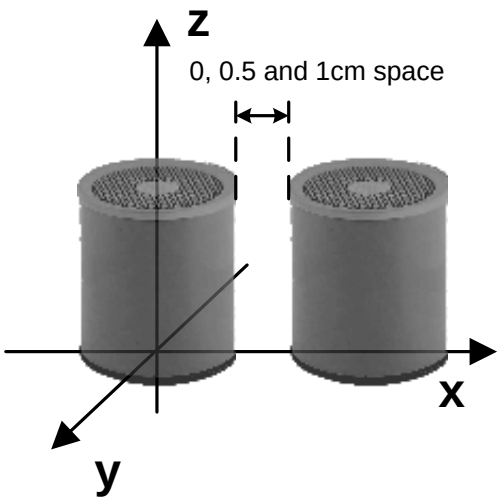

Figure 4.13: Configuration of simulations for determining the spacing between elements

Therefore, the force field produced by two adjacent electromagnets with different spacings are simulated, and the forces along the x-axis demonstrated in Fig. 4.13 are measured at 1cm and 2cm above the top of the elements.

Fig. 4.14 show the force field differences among three spacing strategies, which are 0cm, 0.5cm, and 1cm spacing in between; the current values are both set to 1A.

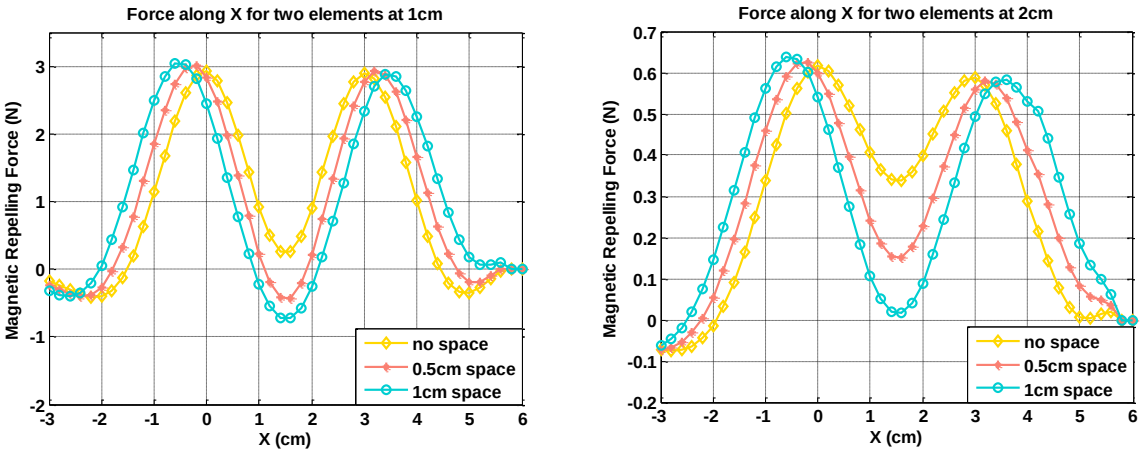

(a) 1cm above

(b) 2cm above

Figure 4.14: Force along X for two elements at different distances

The simulation result clearly shows that the magnetic force superposition effect attenuates with the spacing at both vertical distances. All three arrangements preserve the desired

peak force along the axes of the two elements, and the force drops the least in between the two elements when there is no spacing. Thus, the arrangement of the electromagnet array is determined as the square layout and with no space between the elements.

4.3 Control of the Magnetic Field

4.3.1 Linearity of the System Characteristics

Having the M by K electromagnet array designed, control methods need to be developed to render certain 3D surfaces haptically. For the 3D surface data, no matter if it is static or dynamic, the generated magnetic field will be a static or slowly changing field, which means in a short time slot, the magnetic field can be seen as static. The proposed magnetic rendering control processes for the $N = M \times K$ elements are shown in Fig. 4.15.

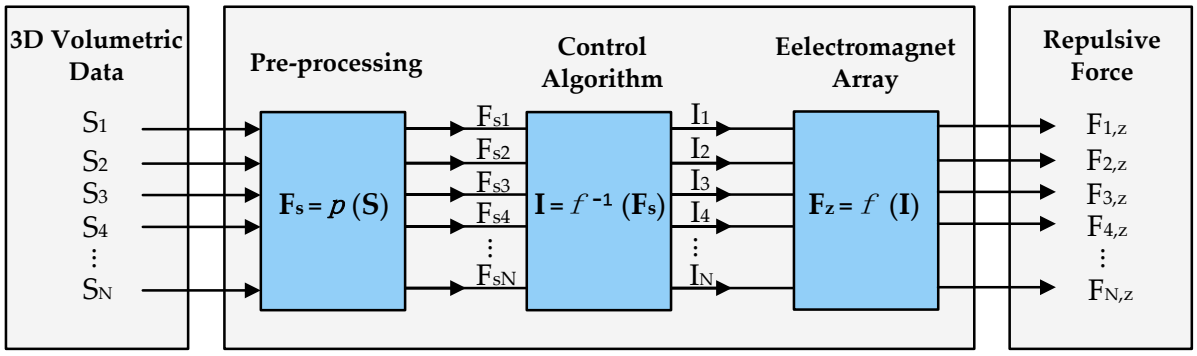

Figure 4.15: Magnetic rendering control processes

The expected forces F_{s} are obtained by sampling and rescaling the 3D surface data $\mathbf{S}$ using certain function $p(\mathbf{S})$, and the electromagnet array is seen as a current-to-force transformation process denoted by $f(\mathbf{I})$, which depends on the electromagnet array model and the vertical distance between the magnet disc and the array. The control algorithm then needs to produce the current values of all the elements based on the expected forces and $f(\mathbf{I})$. Note that force is a vector, and here the vertical component of the magnetic force at the distance of 1cm is used as the control points when developing the control algorithm.

At a certain time, the electromagnet array can be viewed as a MIMO system where each output vertical force relates to all the input currents,

$$F_{\mathrm{i,z}} \triangleq f_{\mathrm{i}}(I_1, I_2, I_3 \dots I_{\mathrm{N}}), \quad i = 1, 2, 3 \dots N, \tag{4.12}$$

where $f_{\mathrm{i}}(i = 1, 2, 3 \dots N)$ are N unknown functions, which depending on the system, need to be determined to model the system.

Assume the N elements with current I_{j}, $(j = 1, 2, 3 \dots N)$ can generate a magnetic field in the location of the ith magnet disc $(i = 1, 2, 3 \dots N)$ individually along the direction of z as

$$B_{\mathrm{i,j,z}} \triangleq g_{\mathrm{i,j}}(I_{\mathrm{j}}), \quad i = 1, 2, 3 \dots N, \quad j = 1, 2, 3 \dots N \tag{4.13}$$

where $g_{\mathrm{i,j}}$ is a function depending on the designed electromagnet model. By substituting in Eq. 4.13 into Eq. 4.1, the magnetic force caused by the jth electromagnet on the ith magnet disc can be obtained as

$$\begin{aligned} F_{\mathrm{i,j,z}} &= \int_{\Omega} M_{\mathrm{disc}} \cdot \frac{\partial B_{\mathrm{i,j,z}} \vec{z}}{\partial z} dV \\ &= \int_{\Omega} M_{\mathrm{disc}} \cdot \frac{\partial g_{\mathrm{i}}(I_{\mathrm{j}}) \vec{z}}{\partial z} dV. \\ &\triangleq h_{\mathrm{i,j}}(I_{\mathrm{j}}) \end{aligned} \tag{4.14}$$

When considering all the elements in the array, because the magnetic field superposition principle states that the total magnetic field generated by multiple separated sources is equal to the sum of the fields generated by each individual source as in Eq. 4.13, the total magnetic field in the location of magnet disc i along the direction of z generated can then be represented as

$$B_{\mathrm{i,z}} = \sum_{j=1}^{N} B_{\mathrm{i,j,z}} = \sum_{j=1}^{N} g_{\mathrm{i}}(I_{\mathrm{j}}). \tag{4.15}$$

By substituting in Eq. 4.15 into Eq. 4.1 the expression of the total magnetic force caused by all the electromagnet on the ith disc can be obtained as

$$\begin{aligned} F_{\mathrm{i,z}} &= \int_{\Omega} M_{\mathrm{disc}} \cdot \frac{\partial B_{\mathrm{i,z}} \vec{z}}{\partial z} dV \\ &= \int_{\Omega} M_{\mathrm{disc}} \cdot \frac{\partial \left(\sum_{j=1}^{N} g_{\mathrm{i}}(I_{\mathrm{j}}) \right) \vec{z}}{\partial z} dV \\ &= \sum_{j=1}^{N} \left(\int_{\Omega} M_{\mathrm{disc}} \cdot \frac{\partial g_{\mathrm{i}}(I_{\mathrm{j}}) \vec{z}}{\partial z} dV \right) \\ &= \sum_{j=1}^{N} h_{\mathrm{i,j}}(I_{\mathrm{j}}) = f_{\mathrm{i}}(I_1, I_2, I_3 \ldots I_{\mathrm{N}}). \end{aligned} \tag{4.16}$$

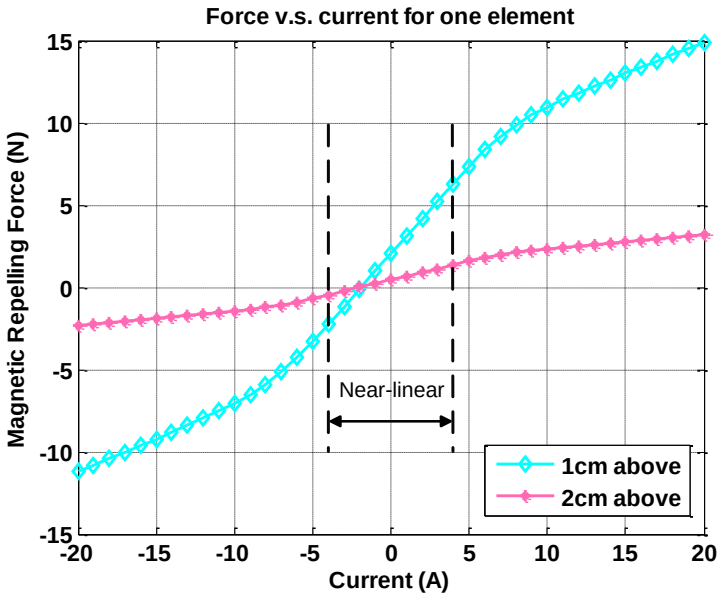

Figure 4.16: Force-current curve for one electromagnet

From the above analysis, it can be seen that the total force caused by multiple current sources $I_{\mathrm{j}}, (j = 1, 2, 3 \ldots N)$ is a summation of $h_{\mathrm{i,j}}(I_{\mathrm{j}})$. Thus, the function $h_{\mathrm{i,j}}(I_{\mathrm{j}})$ needs to be determined. For this purpose, simulations are done for one electromagnet stimulated by current from -20A to 20A, and the corresponding forces are measured at 1cm and 2cm vertical distances. The force-current curves are shown in Fig. 4.16.

From Fig. 4.16, it can be seen that the force is non-linear with the current in a large

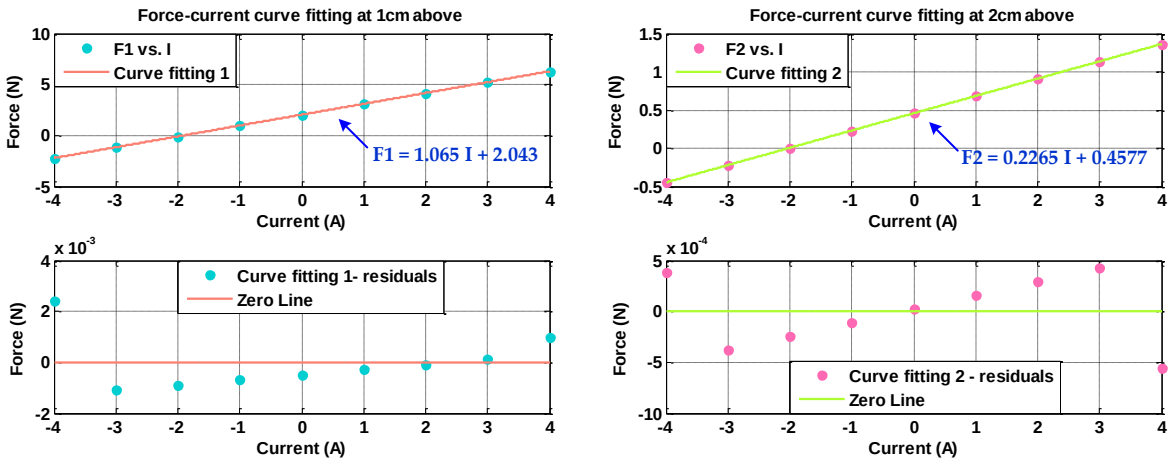

(a) 1cm above

(b) 2cm above

Figure 4.17: Force-current curve of fitting at different distances

range due to the non-linearity of the electromagnet core; however, for the current range $[-4\text{A}, 4\text{A}]$, the curve is near linear. Note that the forces produced when there is no current are not zero due to the permanent magnet concentrator. To verify this assumption, polynomial curve fittings with a degree of 1 are done using the method of least squares which minimizes the RSS. The fitting results are shown together with the residuals in Fig. 4.17a and Fig. 4.17b.

For the precision of the fittings, statistics of the fittings including the 95% confidence intervals and mean square errors (MSE) are calculated and listed in Table 4.2.

Table 4.2: Force-current curve fitting results

Curve	Fitting Model	Coefficients and 95% Confidence Interval	MSE
$F1$ vs.I	$F1 = \alpha_1 I + \beta_1$	$\alpha_1 = 1.065(1.065, 1.066)$ $\beta_1 = 2.043(2.042, 2.044)$	1.059×10^{-6}
$F2$ vs.I	$F2 = \alpha_2 I + \beta_2$	$\alpha_2 = 0.2265(0.2264, 0.2266)$ $\beta_2 = 0.4577(0.4574, 0.4579)$	1.070×10^{-7}

Here confidence intervals of coefficients are 95% confidence bounds calculated by

$$C = p \pm t\frac{\sigma}{\sqrt{n}} \tag{4.17}$$

where p is the resulting coefficients of the fitting, and t is the confidence coefficient depending on the confidence level, which is obtained by inversing the student's t cumulative distribution function. σ is the standard deviation of the sample, and n is the size of sample.

From the fitting results, it can be seen that the linear curve fitting error is negligible, thus the magnetic force is almost proportional to the current value within the range $[-4\mathrm{A}, 4\mathrm{A}]$, and as is mentioned before, the current capacity of the wire is $[-1\mathrm{A}, 1\mathrm{A}]$, which falls in the near-linear range. Thus, the relationship between the vertical force on the ith disc above the element along the axis caused by the jth electromagnet can be modelled with a linear function

$$\begin{aligned} F_{\mathrm{i,j,z}} &= h_{\mathrm{i,j}}(I_{\mathrm{j}}) \\ &\triangleq \alpha_{\mathrm{ij}} I_{\mathrm{j}} + \beta_{\mathrm{ij}}, i, j = 1, 2, 3 \ldots N, \quad I_{\mathrm{j}} \in [-1\mathrm{A}, 1\mathrm{A}] \end{aligned} \tag{4.18}$$

where α_{ij} and β_{ij} are coefficients depending on the locations of the source electromagnet and the magnet disc.

Finally, by substituting Eq. 4.18 into Eq. 4.16, the total force caused by all the electromagnets on the ith magnet disc can be modelled as

$$\begin{aligned} F_{\mathrm{i,z}} &= \sum_{j=1}^{N} h_{\mathrm{i,j}}(I_{\mathrm{j}}) \\ &= \sum_{j=1}^{N} (\alpha_{\mathrm{ij}} I_{\mathrm{j}} + \beta_{\mathrm{ij}}) = \sum_{j=1}^{N} \alpha_{\mathrm{ij}} I_{\mathrm{j}} + \sum_{j=1}^{N} \beta_{\mathrm{ij}}. \end{aligned} \tag{4.19}$$

The above equation can be rewritten using the matrix expression as

$$\begin{bmatrix} F_{1,z} \\ F_{2,z} \\ \vdots \\ F_{N,z} \end{bmatrix} = \begin{bmatrix} \alpha_{11} & \alpha_{12} & \dots & \alpha_{1N} \\ \alpha_{21} & \alpha_{22} & \dots & \alpha_{2N} \\ \vdots & \vdots & & \vdots \\ \alpha_{N1} & \alpha_{N2} & \dots & \alpha_{NN} \end{bmatrix} \begin{bmatrix} I_1 \\ I_2 \\ \vdots \\ I_N \end{bmatrix} + \begin{bmatrix} \beta_1 \\ \beta_2 \\ \vdots \\ \beta_N \end{bmatrix}, \tag{4.20}$$

which can be further simplified as the following linear transformation:

$$\mathbf{F}_z = \mathbf{M}_{\text{trans}}\mathbf{I} + \mathbf{b} \tag{4.21}$$

Here, $\mathbf{M}_{\text{trans}}$ is an N-by-N transformation matrix and $\mathbf{F}_z$, $\mathbf{I}$, and $\mathbf{b}$ are N-by-1 column vectors.

To validate this model, simulations are performed with two electromagnets and the repulsive magnetic force along the axes of both elements at the distance of 1cm and 2cm above are calculated using Eq. 4.1 which, as depicted in Fig. 4.18 and Fig. 4.19.

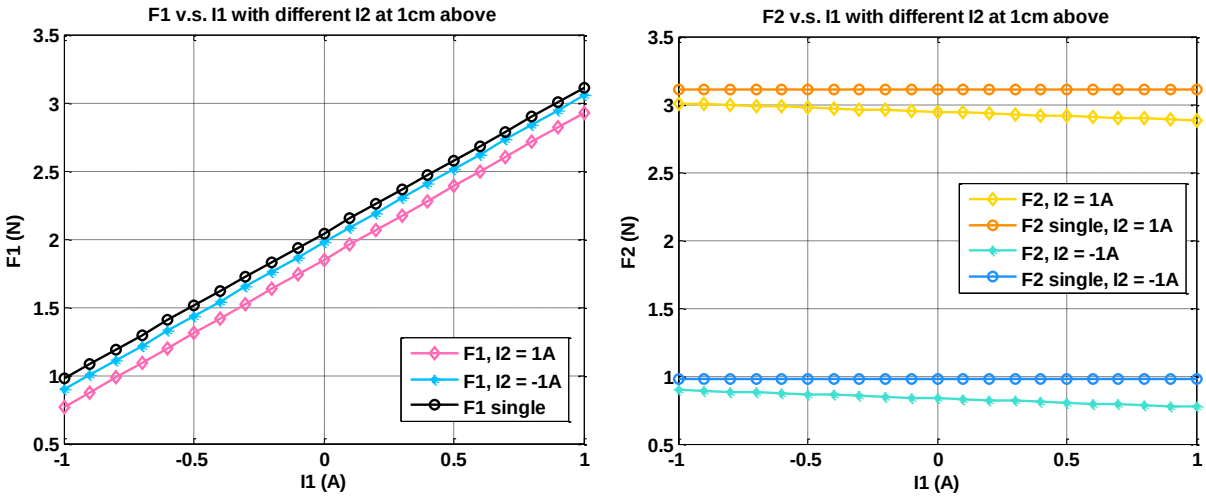

(a) F_1 with $I_1 = 1$A and $I_2 = \pm 1$A (b) F_2 with $I_1 = 1$A and $I_2 = \pm 1$A

Figure 4.18: Force-current curve of two elements at 1cm above

In Fig. 4.19 the vertical forces at 1cm and 2cm above the electromagnets are simulated with I_1 1A and I_2 $\pm$1A. The calculated forces are compared to the simulation of only one element. It can be seen each of the forces depend on both current values, and the resulting forces are a linear combination of both currents, which is consistent with our derivations.

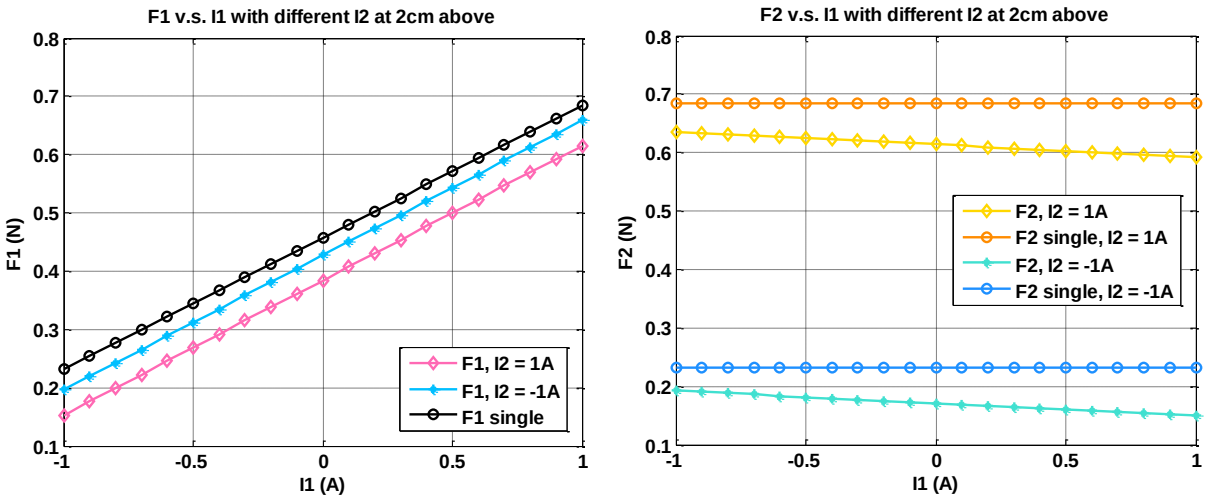

(a) F_1 with $I_1 = 1\text{A}$ and $I_2 = \pm 1\text{A}$ (b) F_2 with $I_1 = 1\text{A}$ and $I_2 = \pm 1\text{A}$

Figure 4.19: Force-current curve of two elements at 2cm above

By this point, the process of data-to-current-to-force transformation has been determined for the electromagnet array containing $N = M \times K$ elements, which is shown in Fig. 4.20.

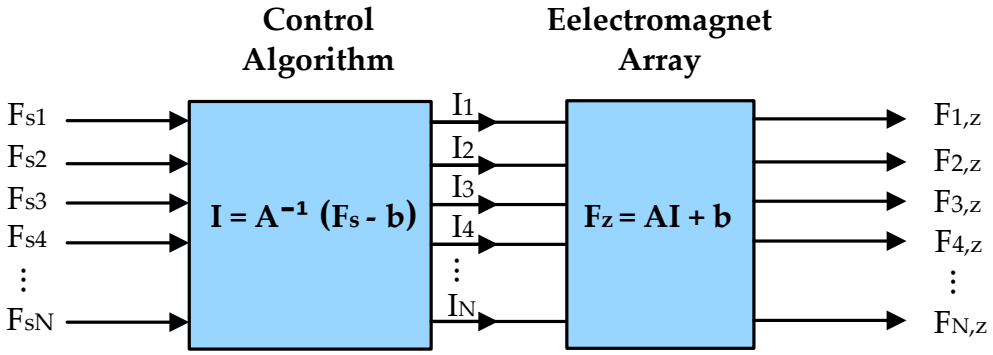

Figure 4.20: Electromagnet array as MIMO process

Based on this model, three control methods are introduced, which will be described in detail in the following sections.

4.3.2 Direct Control

Although each vertical force is affected by all the electromagnets, from Fig. 4.18 and Fig. 4.19, it can be seen that the influence of the surrounding elements is relatively small

compared with the one underneath the magnet disc. The direct control method means that the model is reduced to N linear processes regardless of the interference caused by other elements. The vertical force expression then becomes

$$F_{\mathrm{i,z}} = \alpha I_{\mathrm{i}} + \beta, \quad (i = 1, 2, 3 \ldots N) \tag{4.22}$$

where α and β are constants depending on the vertical distance from the array to the magnet disc. Therefore, by determining α and β using linear curve fitting, direct control can be applied with limited precision.

4.3.3 Control by Batch Model System Identification Techniques

Because the function of the electromagnet array can be regarded as a linear transformation from a set of current values to a set of output vertical forces, the problem falls into the area of system identification. Linear regression techniques are applied that can facilitate identification with respect to several inputs simultaneously as has been introduced in Chapter 3, section 3.3.

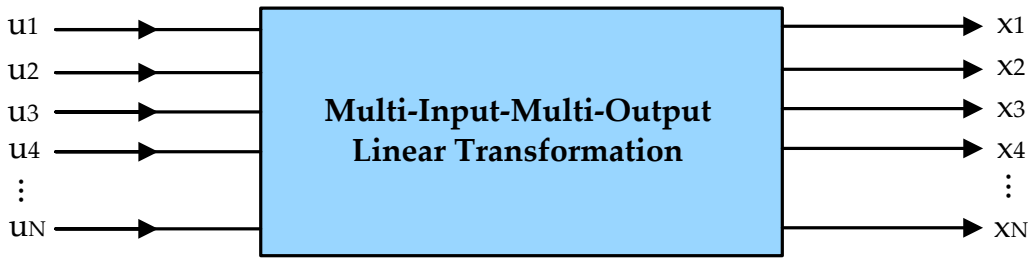

Figure 4.21: MIMO system identification

Recall the force expression for one magnet disc is

$$F_{\mathrm{i,z}} = \alpha_{\mathrm{i1}} I_1 + \alpha_{\mathrm{i2}} I_2 + \cdots + \alpha_{\mathrm{iN}} I_{\mathrm{N}} + \beta_{\mathrm{i}}, \quad (i = 1, 2 \ldots N), \tag{4.23}$$

which has the identical form with Eq. 3.20. Therefore, to determine all the unknown coefficients, r sets of measurement of $\mathbf{I}_{\mathrm{j}} = [I_{1(\mathrm{j})}, I_{2(\mathrm{j})} \ldots I_{\mathrm{N(j)}}]$ and $\mathbf{F}_{\mathrm{j,z}} = [F_{1(\mathrm{j}),\mathrm{z}}, F_{2(\mathrm{j}),\mathrm{z}} \ldots F_{\mathrm{N(j)},\mathrm{z}}]$

for $j = 1, 2 \ldots r$ are taken, and by defining

$$\begin{aligned} \mathbf{u}_{\mathrm{j}} &\triangleq \mathbf{I}_{\mathrm{j}} - \overline{\mathbf{I}_{\mathrm{j}}} \\ \mathbf{x}_{\mathrm{j}} &\triangleq \mathbf{F}_{\mathrm{j,z}} - \overline{\mathbf{F}_{\mathrm{j,z}}}, \quad j = 1, 2, \ldots r \end{aligned} \tag{4.24}$$

where $\overline{\mathbf{I}_{\mathrm{j}}}$ and $\overline{\mathbf{F}_{\mathrm{j,z}}}$ are the average of $\mathbf{I}_{\mathrm{j}}$ and $\mathbf{F}_{\mathrm{j,z}}$ over the r sets of measurement, Eq. 4.23 becomes

$$x_{\mathrm{i}} = \alpha_{\mathrm{i1}} u_1 + \alpha_{\mathrm{i2}} u_2 + \cdots + \alpha_{\mathrm{iN}} u_{\mathrm{N}}, \quad i = 1, 2 \ldots N. \tag{4.25}$$

The coefficients to be determined are

$$\boldsymbol{\alpha}_{\mathrm{i}} \triangleq \begin{bmatrix} \alpha_{\mathrm{i1}} & \alpha_{\mathrm{i2}} & \ldots & \alpha_{\mathrm{iN}} \end{bmatrix}, \quad i = 1, 2 \ldots N \tag{4.26}$$

whose matrix form is defined as transformation matrix $\mathbf{M}_{\mathrm{trans}}$

$$\mathbf{M}_{\mathrm{trans}} \triangleq \begin{bmatrix} \boldsymbol{\alpha}_1 \\ \boldsymbol{\alpha}_2 \\ \vdots \\ \boldsymbol{\alpha}_{\mathrm{N}} \end{bmatrix} = \begin{bmatrix} \alpha_{11} & \alpha_{12} & \ldots & \alpha_{1\mathrm{N}} \\ \alpha_{21} & \alpha_{22} & \ldots & \alpha_{2\mathrm{N}} \\ \vdots & \vdots & & \vdots \\ \alpha_{\mathrm{N}1} & \alpha_{\mathrm{N}2} & \ldots & \alpha_{\mathrm{NN}} \end{bmatrix}. \tag{4.27}$$

For the r sets of measurement, by defining

$$\begin{aligned} \mathbf{X}_{\mathrm{i}} &\triangleq \begin{bmatrix} x_{\mathrm{i(1)}} & x_{\mathrm{i(2)}} & \ldots & x_{\mathrm{i(r)}} \end{bmatrix}^T \\ \mathbf{U} &\triangleq \begin{bmatrix} \mathbf{u}_{(1)}^T \\ \mathbf{u}_{(2)}^T \\ \vdots \\ \mathbf{u}_{(\mathrm{r})}^T \end{bmatrix} = \begin{bmatrix} u_{1(1)} & u_{2(1)} & \ldots & u_{\mathrm{N}(1)} \\ u_{1(2)} & u_{2(2)} & \ldots & u_{\mathrm{N}(2)} \\ \vdots & \vdots & & \vdots \\ u_{1(\mathrm{r})} & u_{2(\mathrm{r})} & \ldots & u_{\mathrm{N}(\mathrm{r})} \end{bmatrix}, \end{aligned} \tag{4.28}$$

the ith output of the r sets of measurement satisfy

$$
\begin{aligned}
x_{\mathrm{i}(1)} &= \boldsymbol{\alpha}_{\mathbf{i}}\mathbf{u}_{(1)} \\
x_{\mathrm{i}(2)} &= \boldsymbol{\alpha}_{\mathbf{i}}\mathbf{u}_{(2)} \\
\cdots &\qquad \cdots \\
x_{\mathrm{i}(\mathrm{r})} &= \boldsymbol{\alpha}_{\mathbf{i}}\mathbf{u}_{(\mathrm{r})}
\end{aligned}
\tag{4.29}
$$

Because Eq. 4.29 is fully analogous to Eq. 3.24 for the single-output case, the best estimates $\hat{\boldsymbol{\alpha}}_{\mathbf{i}}$ of $\boldsymbol{\alpha}_{\mathbf{i}}$ for $\forall i$, in a least-squares regression sense is

$$
\hat{\boldsymbol{\alpha}}_{\mathbf{i}}{}^{T} \triangleq \begin{bmatrix} \hat{\alpha_{1\mathrm{i}}} & \hat{\alpha_{2\mathrm{i}}} & \ldots & \hat{\alpha_{\mathrm{Ni}}} \end{bmatrix}^{T} = (\mathbf{U}^{T}\mathbf{U})^{-1} \cdot \mathbf{U}^{T}\mathbf{X}_{\mathrm{i}}, \tag{4.30}
$$

and the estimated transformation matrix is then

$$
\hat{\mathbf{M}}_{\mathrm{trans}} = \begin{bmatrix} \hat{\boldsymbol{\alpha}}_{\mathbf{1}}{}^{T} & \hat{\boldsymbol{\alpha}}_{\mathbf{2}}{}^{T} & \ldots & \hat{\boldsymbol{\alpha}}_{\mathbf{N}}{}^{T} \end{bmatrix}. \tag{4.31}
$$

For the choice of the r sets of measurement, the matrix $\mathbf{U}^{T}\mathbf{U}$ must be guaranteed as invertible, which means r has to be equal or greater than N.

4.3.4 Adaptive Control

Although Eq. 4.30 provides an adequate method to solve the transformation matrix as a least-squares problem, it is only valid when all the r $(r \geq N)$ sets of measurement are obtained.

To estimate the parameters of the unknown MIMO linear system recursively, adaptive filtering is adopted because it can adjust its parameters according to an adaptive algorithm to find the filter coefficients. The Recursive Least Squares (RLS) method [38], which aims to minimize a weighted least-squares cost function, is applied for its fast convergence.

Fig. 4.22 shows the block diagram of an adaptive control system where the estimated parameters are updated based on the adaptive algorithm.

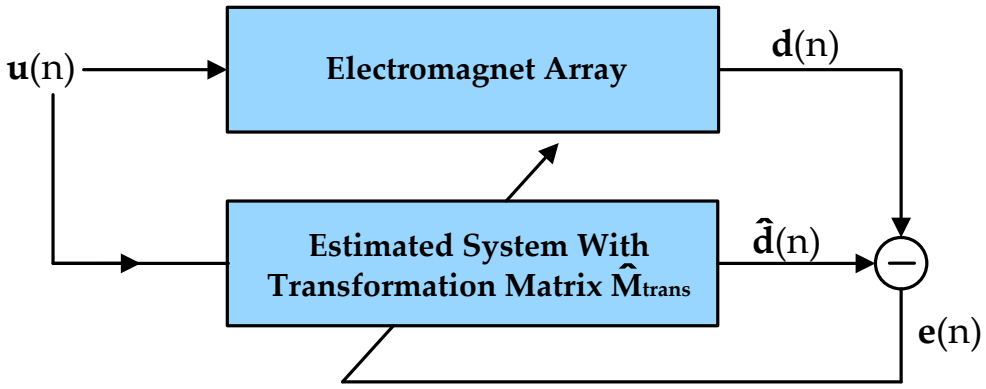

Figure 4.22: Adaptive control

Problem Formulation

As shown in Fig. 4.22, the demeaned input currents and the output vertical forces are denoted as $\mathbf{u}$ and $\mathbf{d}$, which are $N \times 1$ vectors. Here the MIMO linear transformation matrix $\hat{\boldsymbol{M}}_{\text{trans}}$ is to be estimated, which is of size N × N.

The RLS problem formulation in our design is the following:

- Given observations at time n: $\mathbf{u}(n)$ and $\mathbf{d}(n), n = 0, 1 \ldots r$, where r is the total simulation steps
- Determine: $\hat{\boldsymbol{M}}_{\text{trans}}$ that minimizes

$$\mathcal{E}(n) = \sum_{i=0}^{n} \lambda^{n-i} \|\mathbf{e}(i)\|^2 \tag{4.32}$$

where $0 < \lambda \leq 1$ is the forgetting factor that gives older errors exponentially less weight, and $\mathbf{e}(n) = \mathbf{d}(n) - \hat{\mathbf{d}}(n) = \mathbf{d}(n) - \hat{\boldsymbol{M}}_{\text{trans}}(n)\mathbf{u}(n)$ is the error vector at the simulation step n.

RLS Solution Derivation

Minimization of $\mathcal{E}$ with respect to $\hat{\boldsymbol{M}}_{\text{trans}}$ yields the solution according to Wiener-Hopf equations [39]

$$\mathbf{R}(n)\hat{\boldsymbol{M}}_{\text{trans}}(n) = \mathbf{D}(n) \tag{4.33}$$

where $\mathbf{R}(n)$ is the deterministic correlation matrix for input

$$\mathbf{R}(n) \triangleq \sum_{i=0}^{n} \lambda^{n-i}\mathbf{u}(i)\mathbf{u}^T(i), \tag{4.34}$$

and $\mathbf{D}(n)$ is the deterministic cross-correlation vector between the input and desired output

$$\mathbf{D}(n) \triangleq \sum_{i=0}^{n} \lambda^{n-i}\mathbf{u}(i)\mathbf{d}^T(i). \tag{4.35}$$

Note that the update rules of $\mathbf{R}(n)$ and $\mathbf{D}(n)$ can be derived from Eq. 4.34 and Eq.4.35:

$$\mathbf{R}(n) = \lambda\mathbf{R}(n-1) + \mathbf{u}(n)\mathbf{u}^T(n) \tag{4.36}$$

$$\mathbf{D}(n) = \lambda\mathbf{D}(n-1) + \mathbf{u}(n)\mathbf{d}^T(n) \tag{4.37}$$

Thus, the solution

$$\hat{\boldsymbol{M}}_{\text{trans}}(n-1) = \mathbf{R}^{-1}(n-1)\mathbf{D}(n-1) \tag{4.38}$$

can be updated to obtain

$$\hat{\boldsymbol{M}}_{\text{trans}}(n) = \mathbf{R}^{-1}(n)\mathbf{D}(n). \tag{4.39}$$

To find the update rule for $\hat{\boldsymbol{M}}_{\text{trans}}(n)$, the old coefficients $\hat{\boldsymbol{M}}_{\text{trans}}(n-1)$ is checked:

$$\mathbf{R}(n)\hat{\boldsymbol{M}}_{\text{trans}}(n-1) = \mathbf{D}(n) - \mathbf{u}(n)(\mathbf{d}(n) - \hat{\boldsymbol{M}}^T_{\text{trans}}(n-1)\mathbf{u}(n)) \tag{4.40}$$

Thus, we have

$$\hat{\boldsymbol{M}}_{\text{trans}}(n) = \hat{\boldsymbol{M}}_{\text{trans}}(n-1) + \mathbf{R}^{-1}(n)\mathbf{u}(n)\boldsymbol{\xi}(n) \tag{4.41}$$

where $\boldsymbol{\xi}(n) \triangleq \mathbf{d}(n) - \hat{\boldsymbol{M}}_{\text{trans}}^{T}(n-1)\mathbf{u}(n)$ is called the *a priori* error, which is the error at time n if $\hat{\boldsymbol{M}}_{\text{trans}}(n-1)$ is used.

Define the gain vector as

$$\mathbf{K}(n) \triangleq \mathbf{P}(n)\mathbf{u}(n) \tag{4.42}$$

where $\mathbf{P}(n) \triangleq \mathbf{R}^{-1}(n)$. Then, Eq. 4.41 becomes

$$\hat{\boldsymbol{M}}_{\text{trans}}(n) = \hat{\boldsymbol{M}}_{\text{trans}}(n-1) + \mathbf{K}(n)\boldsymbol{\xi}(n). \tag{4.43}$$

By substituting Eq. 4.36 into Eq. 4.42, we get

$$\mathbf{K}(n) = \frac{\lambda^{-1}\mathbf{P}(n-1)\mathbf{u}(n)}{1 + \lambda^{-1}\mathbf{u}^{T}(n)\mathbf{P}(n-1)\mathbf{u}(n)}. \tag{4.44}$$

To avoid matrix inversion, the matrix inversion lemma [44] is applied:

$$\mathbf{P}(n) = \lambda^{-1}\mathbf{P}(n-1) - \lambda^{-1}\mathbf{K}(n)\mathbf{u}^{T}(n)\mathbf{P}(n-1) \tag{4.45}$$

For initialization, normally $\mathbf{P}(0)$ is set to be a diagonal matrix with the non-zero entries being $\delta \gg 1$.

Summary of the RLS Algorithm

The RLS adaptive control algorithm is summarized in Algorithm 1.

The algorithm is known for its fast convergence while its computational complexity is relatively high. To accelerate the convergence of the algorithm, a good first guess is important. Here, for initialization, the fitting result for one element in Fig. 4.17a is used where the interference is not considered, which means the first guess for the transformation matrix is set to be a diagonal matrix whose entries along the diagonal are all 1.065.

Algorithm 1 Recursive Least Squares (RLS) algorithm

Input: $\mathbf{u}(n)$, $\mathbf{d}(n)$

Output: $\hat{\mathbf{M}}_{\text{trans}}$

Initialization: $\delta \leftarrow 100$, $\lambda \leftarrow 0.99999$

$\mathbf{P}(0) \leftarrow \delta\mathbf{I}$, $\hat{\mathbf{M}}_{\text{trans}}(0) \leftarrow \mathbf{0}$

for $n \leftarrow 1$ **to** *maximum iteration* **do**

  $\mathbf{K}(n) \leftarrow \frac{\lambda^{-1}\mathbf{P}(n-1)\mathbf{u}(n)}{1+\lambda^{-1}\mathbf{u}^T(n)\mathbf{P}(n-1)\mathbf{u}(n)}$

  $\boldsymbol{\xi}(n) \leftarrow \mathbf{d}(n) - \hat{\mathbf{M}}^T_{\text{trans}}(n-1)\mathbf{u}(n)$

  $\hat{\mathbf{M}}_{\text{trans}}(n) \leftarrow \hat{\mathbf{M}}_{\text{trans}}(n-1) + \mathbf{K}(n)\boldsymbol{\xi}(n)$

  $\mathbf{P}(n) \leftarrow \lambda^{-1}\mathbf{P}(n-1) - \lambda^{-1}\mathbf{K}(n)\mathbf{u}^T(n)\mathbf{P}(n-1)$

  $\mathbf{e}(n) \leftarrow \mathbf{d}(n) - \hat{\mathbf{M}}^T_{\text{trans}}(n)\mathbf{u}(n)$

  if $\mathbf{e}(n) < threshold$ **then**

    break

  end if

end for

Chapter 5

Simulation and Results

5.1 Simulation Methodology

5.1.1 COMSOL Multiphysics and Livelink for MATLAB

COMSOL Multiphysics is a powerful FEM simulation software for modelling and solving engineering problems with coupled physics [45]. COMSOL Multiphysics provides a desktop graphical user interface environment which has the model builder that allows users to build 2D or 3D models while viewing the model interactively.

All the simulating and analysing functionalities involved in all steps in the modelling process are accessible via the desktop environment, including the following:

- *Parameters setting*, for defining the parameters' values and units used in the model
- *Geometry setting*, for creating the model in either 2D or 3D
- *Material setting*, for assigning built-in or user-defined material to different domains of the model
- *Physics setting*, for specifying proper physics and setting up the physics equations together with boundary conditions

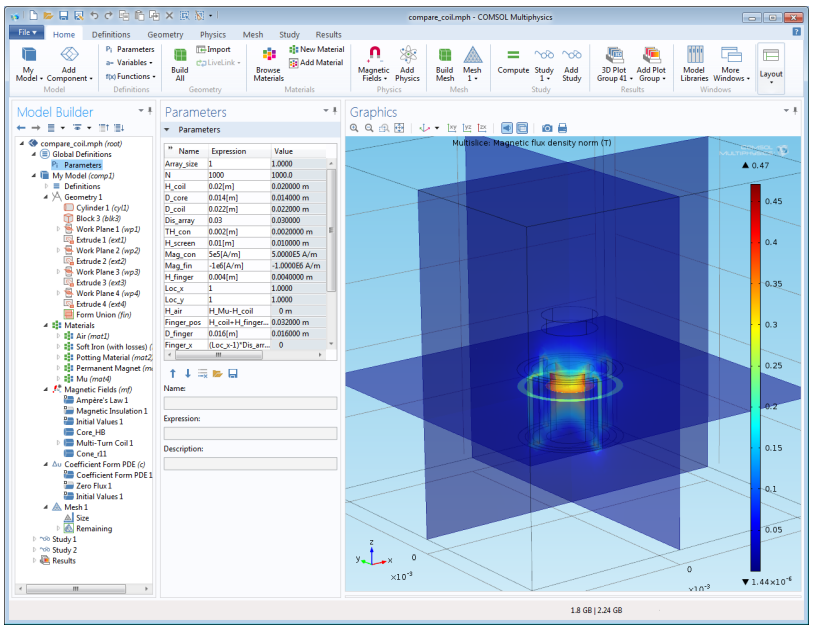

Figure 5.1: COMSOL desktop environment

- *Mesh setting*, for designing the shape and size of meshing for each domain
- *Study setting*, for setting up the study type and sequence for solving the model
- *Result setting*, for post-processing results such as variables evaluation and figures plotting.

In addition, the MATLAB scripting environment is integrated with COMSOL Multiphysics via the LiveLink for MATLAB [46], which provides additional flexibility in generating, running, and processing the model in MATLAB while applying MATLAB functions. Therefore, the whole modelling and simulating process can be done in MATLAB from scratch.

Commands are entered in MATLAB in a Java-based syntax which is supported by the COMSOL Application Programming Interface (API). MATLAB is thus connected to a COMSOL server using a client/server mode, so that whatever objects the user builds in MATLAB exist on the COMSOL server, which means operations and modifications on either side can be updated simultaneously on the other side.

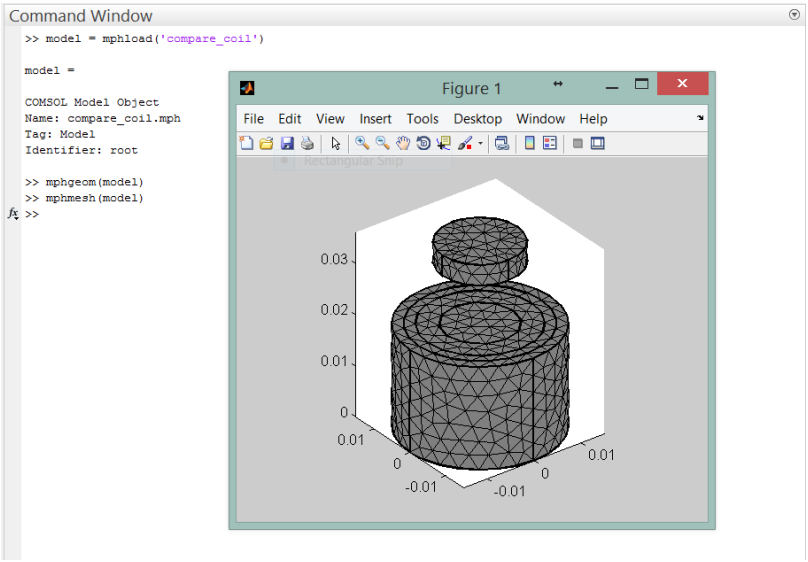

Figure 5.2: LiveLink for MATLAB

5.1.2 Solving the Magnetic Field and the Derivation

To solve the spatial magnetic field in magnetostatics, the physics of the Magnetic Fields in AC/DC module is chosen and Ampere's law in Eq. 3.8 is rewritten with the definition of magnetic potential in Eq. 3.15 and the constitutive relationship in Eq. 3.11:

$$\nabla \times (\mu_0^{-1} \nabla \times \vec{A} - \vec{M}) = \vec{J}. \tag{5.1}$$

In COMSOL, magnetic vector potential $\vec{A}$ is first solved as the dependent variable in the Magnetic Fields Module, and magnetic flux density is then calculated as $\vec{B} = \nabla \times \vec{A}$. For calculating the z component of the magnetic flux derivation, which is needed in force computation in Eq. 4.1, the Δu Coefficient Form PDE module is added to the physics with B_z as the dependent variable. Therefore, two studies are created for these two physics and are executed in order, with B_z passing from the first study to the second.

5.1.3 Field Equations

To solve the magnetic potential using FEM, the domain equations are summarized in Fig. 5.3.

Domain	Equations
1. Surrounding air 2. Magnet disc	$\nabla \times (\mu_0^{-1} \nabla \times \vec{A} - \vec{M}) = \vec{J}$; $\vec{M} = \vec{0}$; $\vec{J} = \vec{0}$
3. Concentrator	$\nabla \times (\mu_0^{-1} \nabla \times \vec{A} - \vec{M}) = \vec{J}$; $\vec{B} = \mu_0(\vec{H} + \vec{M})$; $\vec{M} = -\mathrm{Mag}_{\mathrm{con}} \cdot \vec{r}$; $\vec{J} = \vec{0}$
4. Windings	$\nabla \times (\mu_0^{-1} \nabla \times \vec{A} - \vec{M}) = \vec{J}$; $\vec{J} = \frac{N I_{\mathrm{coil}}}{A} \vec{e_{\mathrm{coil}}}$; $\vec{M} = \vec{0}$
5. Core	$\nabla \times \vec{H} = \vec{J}$; $\vec{H} = f(\lvert\vec{B}\rvert)$; $\vec{J} = \vec{0}$
6. Mu-metal shell	$\nabla \times \vec{H} = \vec{J}$; $\vec{B} = \mu_0 \mu_r \vec{H}$; $\vec{J} = \vec{0}$

Figure 5.3: Domain equations for solving magnetic potential

For the force calculation part, the equation for volume integration is set up in the result as a post-process step as shown in Fig. 5.4.

Domain	Equations
2. Magnet disc	$F_z = \int_\Omega M_{\mathrm{disc}} \cdot \frac{\partial B_z}{\partial z} dV$

Figure 5.4: Domain equations for computing vertical magnetic force

5.2 Electromagnet Simulation Model Setup

5.2.1 Environment Choices for Modelling

For our simulations, we use both the COMSOL desktop environment and the LiveLink for MATLAB for modelling and simulating. The COMSOL desktop environment is used for single electromagnet model building and simulating because the building process is intuitive

and the complexity is relatively low. LiveLink for MATLAB is used for generating and running the electromagnet array model for that the geometry can be built using loops which can greatly facilitate the modelling process for large scale arrays.

5.2.2 Model Building for One Electromagnet

A single electromagnet model is first built in the COMSOL desktop environment. The geometry of the single model is built in 3D by extruding 2D drawings on different work planes to the desired height. Four work planes are defined for the soft iron core, the windings, the permanent magnet concentrator, and the Mu-metal shell respectively, which are all extruded to 3D space by the same height designed for the electromagnet model.

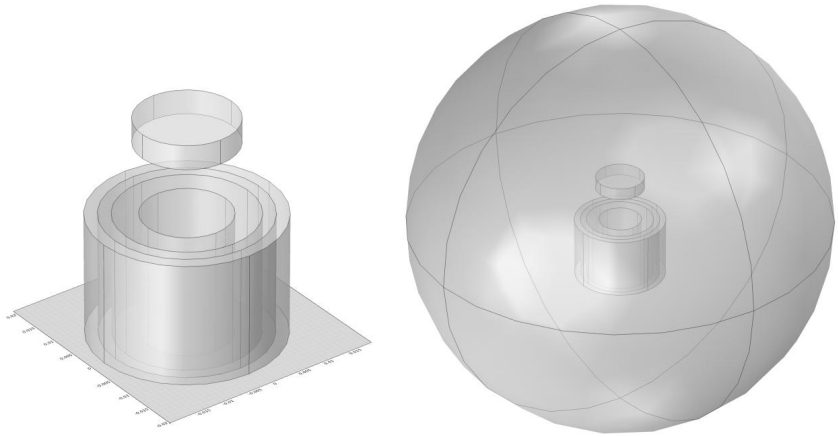

Figure 5.5: Geometry of the designed electromagnet model

The magnet disc above the electromagnet is modelled directly by a cylinder. All domains discussed above are encapsulated in a sphere as the boundary of the whole geometry to be solved.

Two sets of coordinate are defined for the model, one is Cartesian and the other cylindrical. The Cartesian system is used as global boundary coordinate system when specifying the measurements and the locations of the geometry, and the cylindrical system is specifically for defining the magnetization direction of the permanent magnet concentrator. The relationships between the two coordinate systems are depicted in Fig. 5.6.

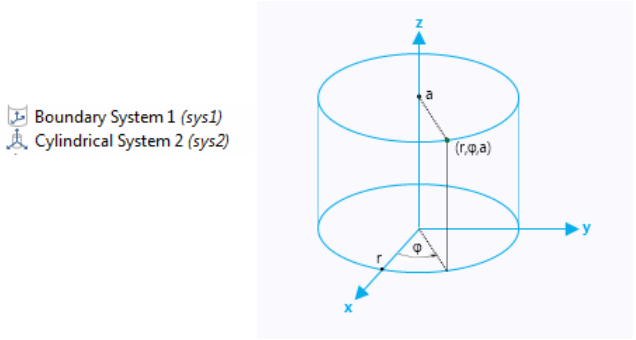

Figure 5.6: Coordinate systems defined for modeling

For boundary conditions and initializations of the simulation, magnetic insulation condition $\vec{n} \times \vec{A} = 0$ is applied on the surface of the sphere as a boundary condition, and initial values $\vec{A} = \vec{0}$ are applied on all domains.

The measurements and material properties are set as listed in Table 4.1. The definition of the geometry domains together with some key settings in material and in physics are shown in Fig. 5.7. Note that the material and physics for the magnet disc is not specified (in real simulations, the material of the magnet discs are set to be air as default), because we are only using the volume of the discs for integration when post-processing as is written in Eq. 4.1 where the magnetization of the disc is truly defined.

5.2.3 Implementation of Force Calculation in COMSOL

To calculate the derivation $\frac{\partial B_z}{\partial z}$, which is needed in computing the vertical magnetic force, the Δu Coefficient Form PDE module is added as the second physics, which is shown in Fig. 5.8. The equation in the PDE module is set as order one derivation whose source is the z component of the magnetic flux density B_z, as shown in Fig. 5.9

Having all the geometry and material properties defined, when the magnetic potential $\vec{A}$ is solved, and the magnetic flux density is calculated, the study for coefficient form PDE can be run to obtain the derivation. Thus, two studies for the two physics are created, both of which are stationary, and settings shown in Fig. 5.10 are made to couple the two via the z component of magnetic flux density.

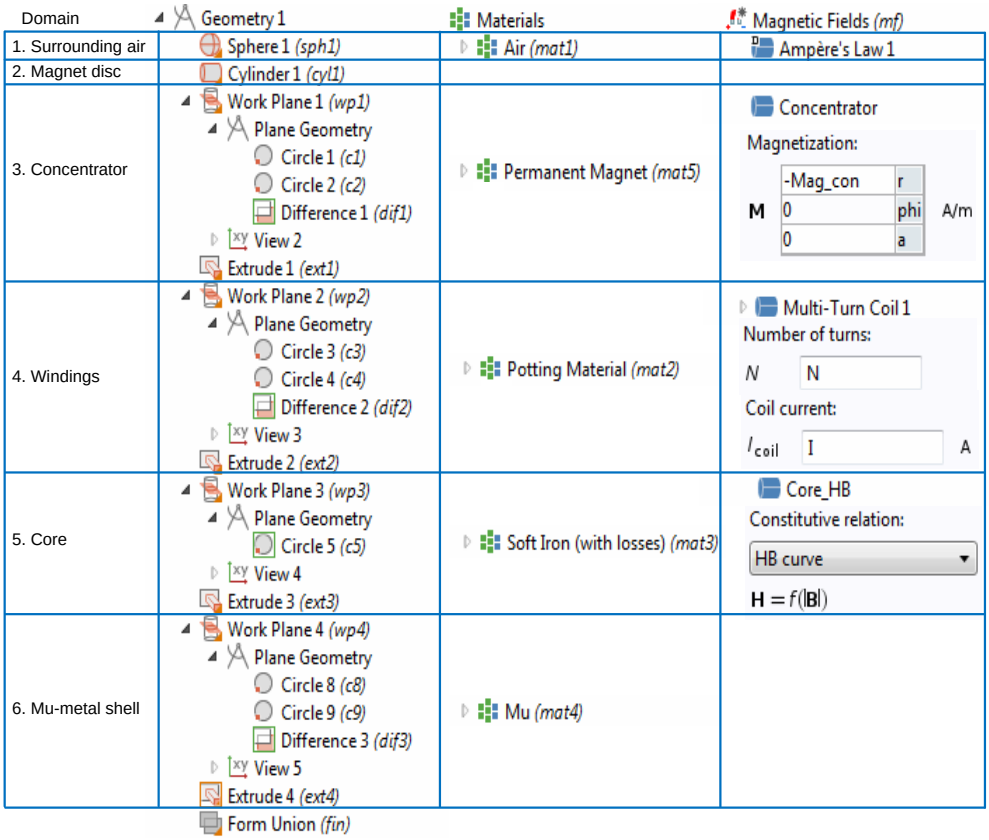

Figure 5.7: Model building in COMSOL

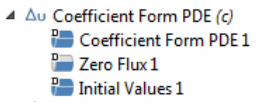

Figure 5.8: The Δu Coefficient Form PDE module

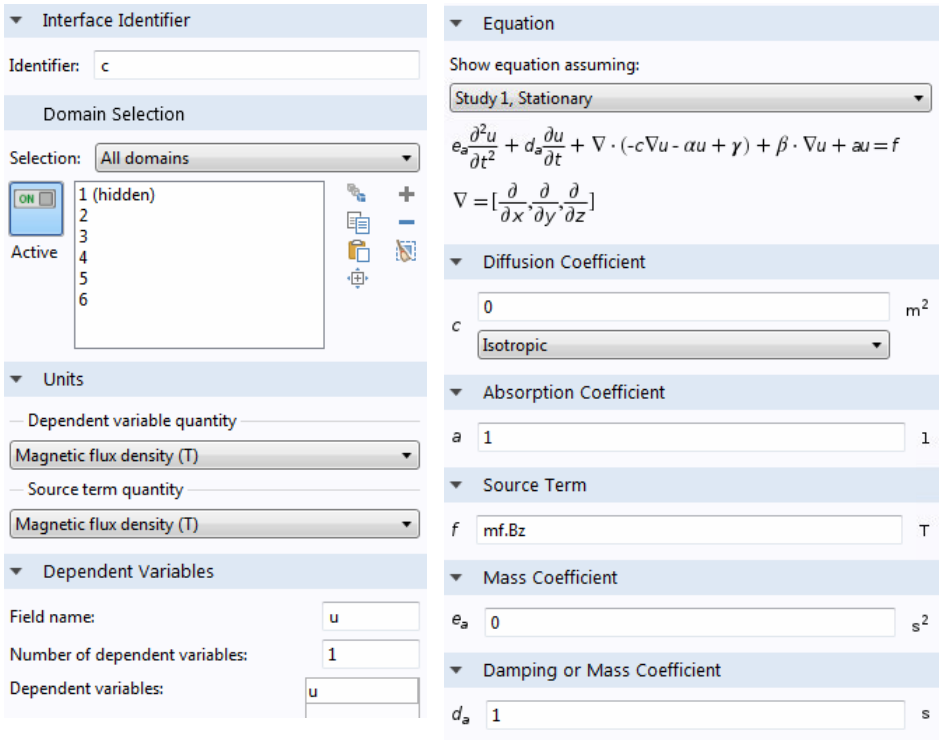

Figure 5.9: Settings of the Δu Coefficient Form PDE module

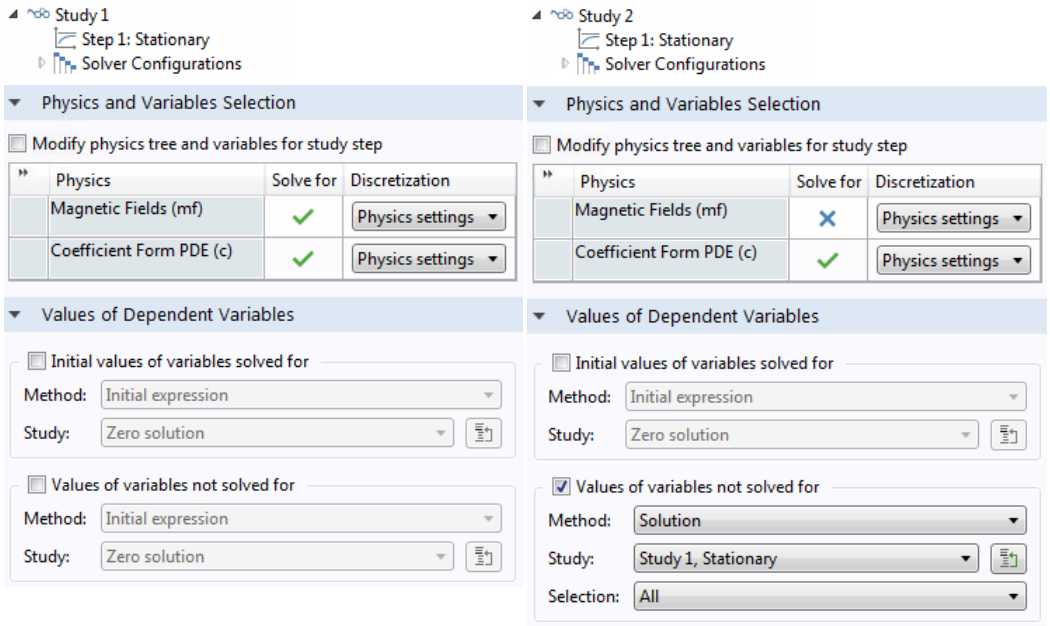

Figure 5.10: Two studies for magnetic fields and coefficient form PDE

Finally, the vertical magnet force is computed by volume integrating $\frac{\partial B}{\partial z}$ over the volume of the magnet disc. This process is done by adding a Volume Integration in the result node of COMSOL, which is shown in Fig. 5.11.

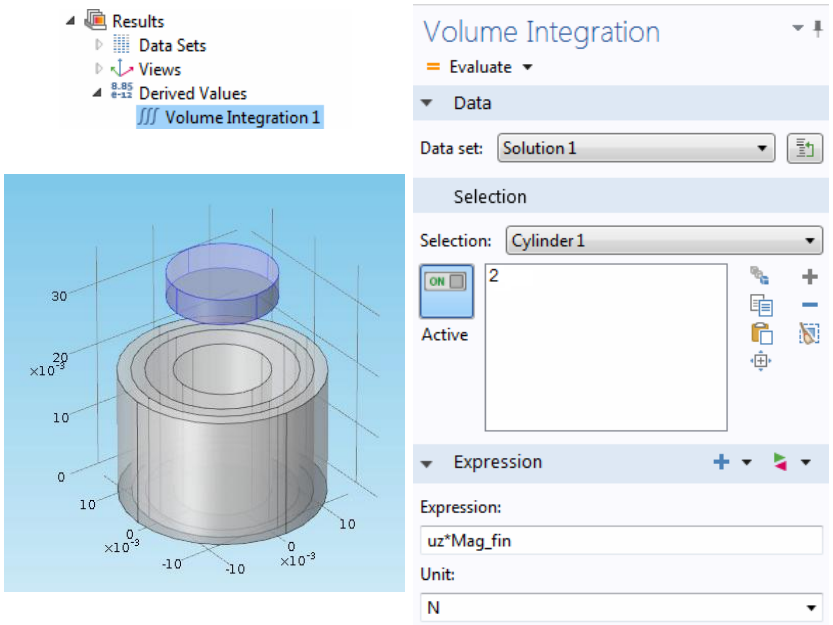

Figure 5.11: Volume integration for computing the magnetic force

5.2.4 Meshing Concerns

FEM divides the whole problem domain geometrically into small simple elements; in our case, the 3D mesh shape is set to be tetrahedrons. Mesh settings need to be done because that determines the resolution of the meshes splitting the model. Because there are small faces in our electromagnet model, the size of mesh is set to be smaller than the default one. This will help in getting a more accurate result when solving the magnetic field potential and the volume integration; however the fineness of mesh and the computational speed are always a pair of trade-off factors.

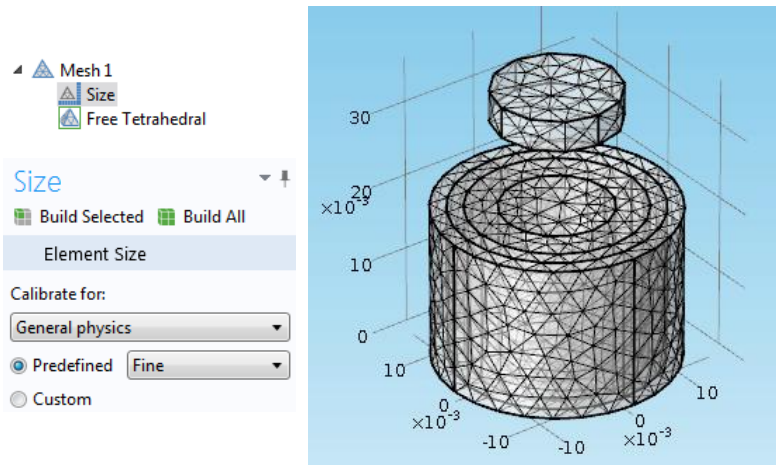

Figure 5.12: Mesh for the geometry

5.3 Performance of the Designed Electromagnet Model

In this section, the magnetic vertical force production performance is compared among the three kinds of models shown in Fig. 4.4:

- *Traditional model*, which is made only of a core and a coil
- *Concentrated model*, which has the magnetic field concentrator added on the traditional model
- *Designed model*, which is the complete model with the Mu-metal shell added on the concentrated model

All of the three models have the same settings for the coil, i.e., the dimensions, the turns of wire and the current value. First, as a performance demonstration for individual electromagnets, the vertical magnetic forces produced by one element at the vertical distances of 1cm and 2cm are simulated. The stimulating current values set in the range of $[-1\text{A}, -1\text{A}]$ with a 0.1A interval and the vertical repulsive forces are obtained using FEM introduced in the previous section. The simulation result is presented in Fig. 5.13.

It can be seen from the results that the force generated is augmented significantly by the introduction of the concentrator and the Mu-metal shell in the designed model.

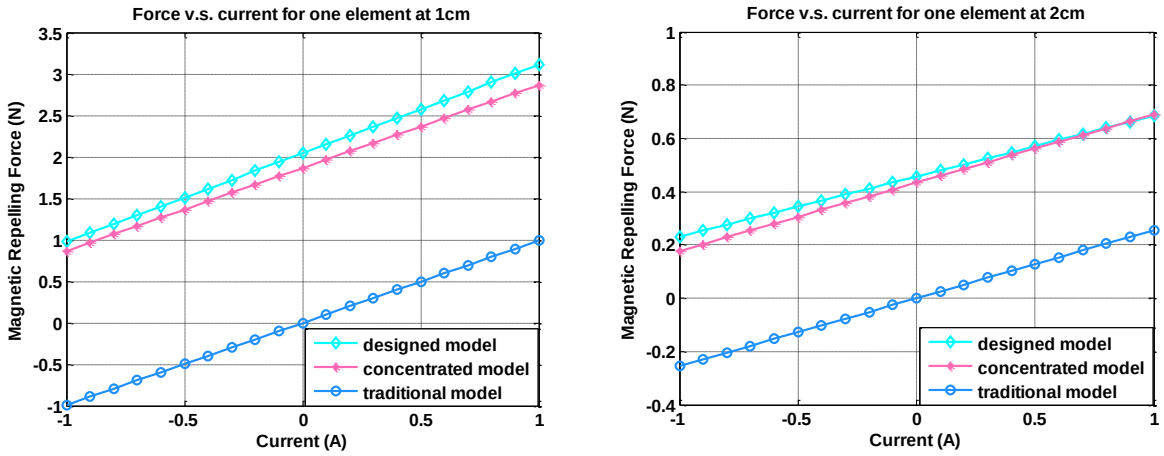

(a) 1cm above

(b) 2cm above

Figure 5.13: Force produced by three models with different current values

From the comparison of the concentrated model with the traditional model, we can see the concentrator functions like an offset of about $1.9N$ at 1cm above and about $0.4N$ at 2cm above. The effect of the offset also ensures the magnetic force generated is repulsive when the current falls in the range of $[-1\text{A}. - 1\text{A}]$. The shielding effect can also be observed in Fig. 5.13a by comparing the designed model with the concentrated model, which further increases the force to some degree not only by offsetting but also increasing the slopes of the line. However the shielding effect becomes weaker with the vertical distance as shown in Fig. 5.13b.

The vertical force generated with the current value set to be 1A at different vertical distances from 0cm to 3cm with 0.1cm intervals are also simulated and compared in Fig. 5.14, and the results in the range of $[1\text{cm}, 2\text{cm}]$ are zoomed in the bottom figure.

The magnetic force drops off with distance, which can be seen from Fig. 5.14. The advantage of force production by the designed model against the other two increases when the distance becomes smaller, and, again, we can see that the shielding effect decreases with the distance.

Next, simulations are done that scan the force generated along the horizontal axis (x-axis) at 1cm and 2cm above. The current value of the three models is set as 1A.

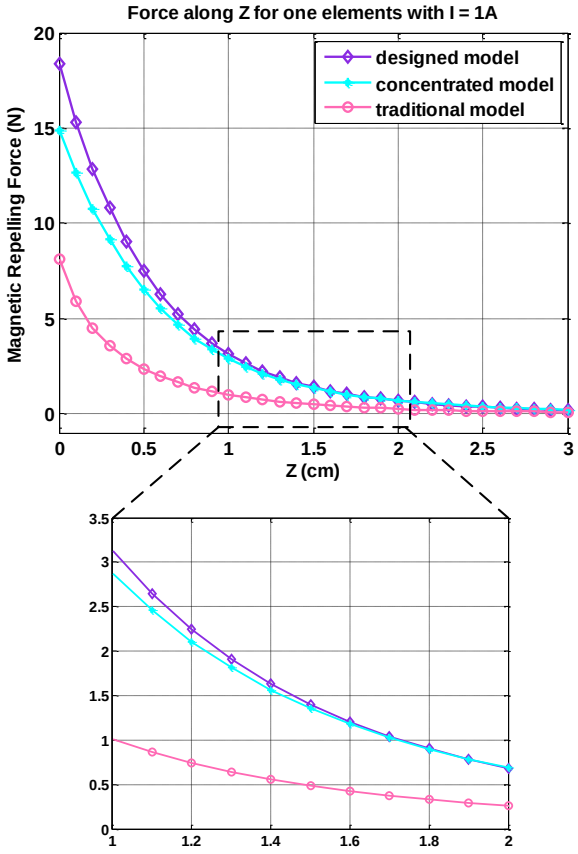

Figure 5.14: Force produced by a 1A current at different vertical distances above

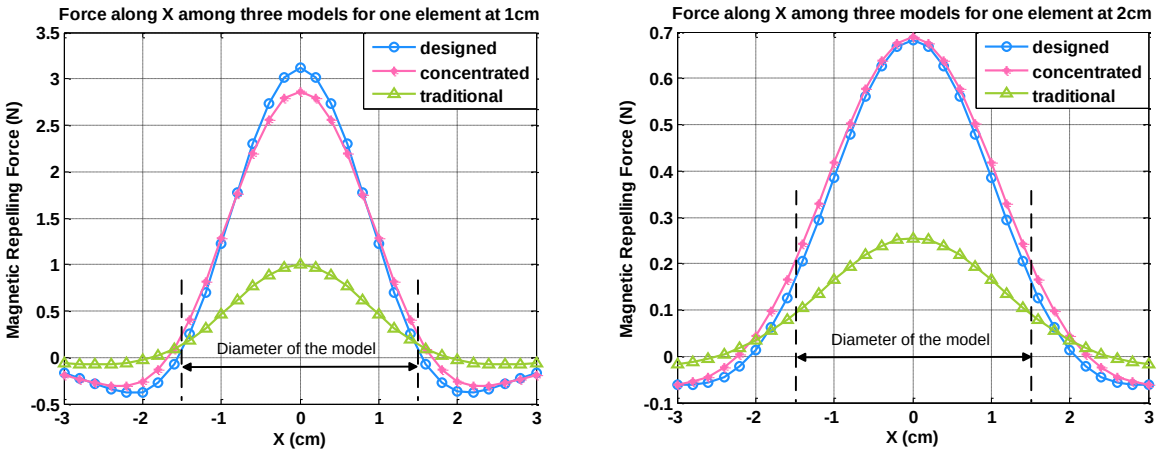

(a) 1cm above (b) 2cm above

Figure 5.15: Force produced along the x-axis by 1A

It can be seen from Fig. 5.15 that the magnetic force forms a bell shape above the element, and the bell for the force generated by the designed model is thinner compared to the other two, indicating the magnetic field is bounded better. Besides that, the bell shapes become wider with the vertical distance above the element, which means the magnetic force field becomes smoother with the distance larger.

To determine the range of vertical distance the force can be perceived, data regarding human hand thresholds for static force are required. According to researched literature, for fingertips, the minimum force that can be perceived is 0.8mN, and for the palm, the threshold is 1.5mN [47]. Thus, the vertical force generated by the designed model with a 1A current at different vertical distances from 0cm to 5.2cm with a 0.1cm interval are simulated and depicted in Fig. 5.16 with the results in the range of $[4\text{cm}, 5.2\text{cm}]$ zoomed in.

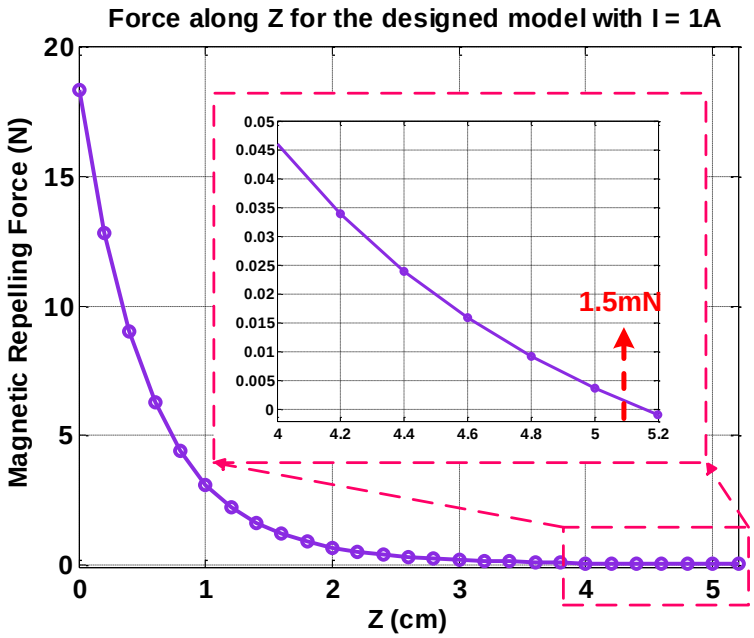

Figure 5.16: Force produced by designed model 1A current at different vertical distances above

Based on the human hand threshold for static force, we find the farthest vertical distance where the force can be felt by both palm and fingertip is about 5.1cm.

Finally, the stiffness of the axial magnetic force K_z can then be calculated using

$$K_z = -\frac{\partial}{\partial z}F = -\frac{d}{dz}F_z \tag{5.2}$$

and is depicted in Fig. 5.17. The degree of stiffness is based on the study of human hand stiffness perception [48] where objects with stiffness higher than $650\text{N}\,\text{mm}^{-1}$ is perceived as very firm, and stiffness between $650\text{N}\,\text{mm}^{-1}$ and $350\text{N}\,\text{mm}^{-1}$ is considered firm and feels like touching a piece of wood lying on foam. Stiffness lower than $350\text{N}\,\text{mm}^{-1}$ is perceived as a soft object.

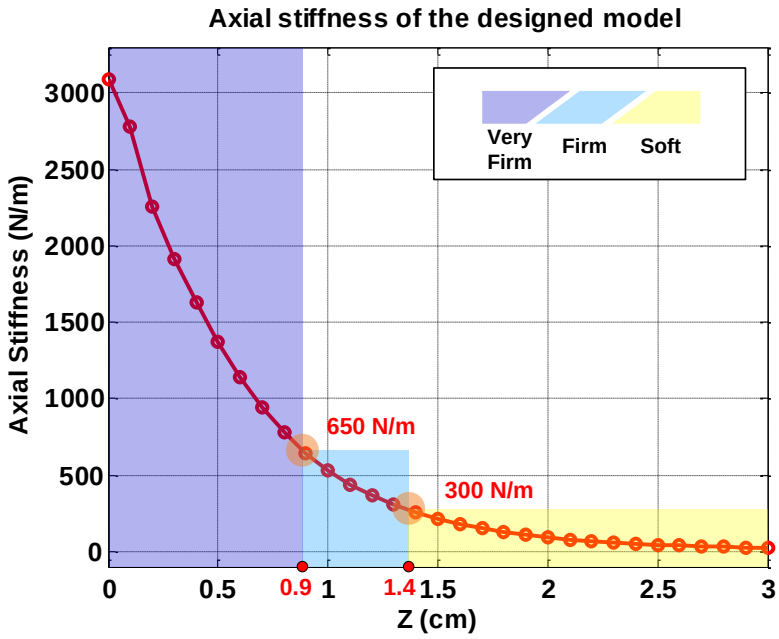

Figure 5.17: Axial stiffness of the designed model

From Fig. 5.17, it can be seen that within the height of 0.9cm, the magnetic force generated can be felt as very firm, and between 0.9cm and 1.4cm above the model, a firm object sensation will be produced, beyond which the force will probably be considered soft.

5.4 Electromagnet Array Control Experiments

5.4.1 Experiments on a 3-by-3 Model

To build the electromagnet array model, an extensive amount of coding associated with modelling and simulating have been done with COMSOL LiveLink for Matlab, which has been made general for flexible array size. The geometry of the 3-by-3 model and its indexing are shown in Fig. 5.18.

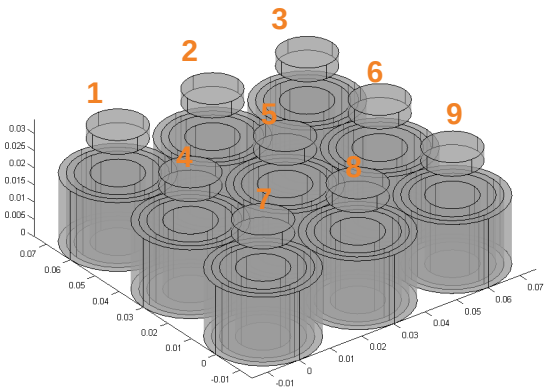

Figure 5.18: Modeling and indexing of a 3-by-3 electromagnet array

The three control methods introduced in Chapter Proposed Method Section Control of the Magnetic Field are implemented in MATLAB and applied to the 3-by-3 model.

Direct Control on the 3-by-3 Model

Direct control is configured based on the fitting result in Table 4.2. The testing force values are set, and the corresponding current values are obtained by simply reversing the fitting equation for the 1cm vertical distance case.

$$\begin{aligned} F_{\mathrm{i,z}} &= 1.065 I_{\mathrm{i}} + 2.043 \\ I_{\mathrm{i}} &= (F_{\mathrm{i,z}} - 2.043)/1.065, \quad i = 1, 2 \ldots 9 \end{aligned} \tag{5.3}$$

The test forces and the current values for direct control for the 3-by-3 model are listed in Table 5.1. Note that the electromagnet indexing is shown in Fig. 5.18.

Table 5.1: Test forces and currents for direct control of 3-by-3 electromagnet array

Index			Force Values (N)			Current Values (A)		
1	2	3	1.0	1.9	2.0	-0.979	-0.134	-0.040
4	5	6	2.2	1.5	2.7	-0.147	-0.510	0.617
7	8	9	1.7	2.3	1.2	-0.322	0.241	-0.792

The above listed current values are configured in the model, and the result obtained from the simulation is presented in Table 5.2.

Table 5.2: Test results for direct control of 3-by-3 electromagnet array

Index	Desired Force (N)	Result Force (N)	Error (N)	Mean Square Error
1	1.0	0.705	0.295	
2	1.9	1.577	0.323	
3	2.0	1.698	0.302	
4	2.2	1.897	0.303	
5	1.5	0.952	0.548	0.1198
6	2.7	2.388	0.312	
7	1.7	1.398	0.302	
8	2.3	1.981	0.319	
9	1.2	0.864	0.336	

Batch Model System Identification for the 3-by-3 Model

To perform the equation based on Eq. 4.30,

$$\hat{\mathbf{M}}_{\text{trans}} = (\mathbf{U}^T\mathbf{U})^{-1} \cdot \mathbf{U}^T\mathbf{X}, \tag{5.4}$$

the input matrix $\mathbf{U}$ and the state matrix $\mathbf{X}$ need to be found. As has been discussed in Chapter 4, section 4.3.3, for a system with N output, $r \geq N$ sets of measurement are needed for batch model system identification to obtain the estimated linear transformation of the

system. For the 3-by-3 electromagnet array model, $N = 9$ and 10 sets of measurement are collected.

To guarantee the matrix $\mathbf{U}^T\mathbf{U}$ is invertible, the 10 sets of simulating currents are selected so that when forming a matrix, its rank is equal to the element number of the array, which is 9, and each current value is changed at least once. The stimulating current sets are showing in Table 5.3.

Table 5.3: Current sets used in batch model system identification

Simulation No.	Current Values (A)								
	I_1	I_2	I_3	I_4	I_5	I_6	I_7	I_8	I_9
1	-1	-1	-1	-1	-1	-1	-1	-1	-1
2	1	1	1	1	1	1	1	1	1
3	-1	-1	-1	-1	-1	-1	-1	-1	1
4	-1	-1	-1	-1	-1	-1	-1	1	1
5	-1	-1	-1	-1	-1	-1	1	1	1
6	-1	-1	-1	-1	-1	1	1	1	1
7	-1	-1	-1	-1	1	1	1	1	1
8	-1	-1	-1	1	1	1	1	1	1
9	-1	-1	1	1	1	1	1	1	1
10	-1	1	1	1	1	1	1	1	1

Thus, the current record matrix with size 10×9 is obtained from Table 5.3 and the force record matrix from the corresponding simulations is shown in Table 5.4. Note that the electromagnet indexing is the same as that of Table 5.1.

Note that according to Eq. 4.24, the current and force record matrices need to be detrended to get the input matrix $\mathbf{U}$ and the state matrix $\mathbf{X}$ to perform Eq. 5.4. Because the current range is set to be $[-1A, 1A]$, the mean value vector for each current $\overline{\mathbf{I}_{\mathrm{i}}}$ is then a zero vector. The mean values for each force measurement $\overline{\mathbf{F}_{\mathrm{i,z}}}$ are estimated by averaging the force measurement $F_{\mathrm{i,z}}$ $(i = 1, 2 \ldots 9)$ over the cases where $I_{\mathrm{i}} = \pm 1A$. Then, the mean vectors discussed above are

Table 5.4: Simulation results of the 3-by-3 electromagnet array for batch model system identification

Simulation No.	Force Values (N)								
	$F_{1,z}$	$F_{2,z}$	$F_{3,z}$	$F_{4,z}$	$F_{5,z}$	$F_{6,z}$	$F_{7,z}$	$F_{8,z}$	$F_{9,z}$
1	0.817	0.770	0.820	0.769	0.712	0.768	0.822	0.767	0.822
2	2.686	2.520	2.691	2.508	2.336	2.522	2.684	2.510	2.667
3	0.815	0.766	0.813	0.765	0.684	0.654	0.815	0.654	2.947
4	0.811	0.760	0.809	0.737	0.575	0.625	0.701	2.804	2.833
5	0.804	0.757	0.807	0.623	0.547	0.622	2.843	2.690	2.826
6	0.800	0.728	0.693	0.617	0.437	2.784	2.839	2.662	2.712
7	0.771	0.618	0.665	0.507	2.610	2.674	2.811	2.552	2.683
8	0.657	0.589	0.661	2.654	2.501	2.668	2.697	2.523	2.679
9	0.650	0.476	2.812	2.650	2.473	2.554	2.695	2.519	2.672
10	0.536	2.634	2.698	2.622	2.364	2.526	2.691	2.513	2.668

$$\overline{\mathbf{I}_{\mathrm{i}}} = \begin{bmatrix} 0 & 0 & 0 & 0 & 0 & 0 & 0 & 0 & 0 \end{bmatrix}^T$$
$$\overline{\mathbf{F}_{\mathrm{i,z}}} = \begin{bmatrix} 1.751 & 1.645 & 1.756 & 1.639 & 1.524 & 1.645 & 1.753 & 1.638 & 1.744 \end{bmatrix}^T \tag{5.5}$$

Thus, the input matrix $\mathbf{U}$ is the same as Table 5.3, and by subtracting each column in Table 5.4 by the corresponding mean value, the state matrix $\mathbf{X}$ is obtained as shown in Table 5.5.

Table 5.5: State matrix $\mathbf{X}$ of batch model system identification for the 3-by-3 model

-0.935	-0.875	-0.936	-0.870	-0.812	-0.877	-0.931	-0.871	-0.922
0.935	0.875	0.936	0.870	0.812	0.877	0.931	0.871	0.922
-0.936	-0.879	-0.943	-0.873	-0.840	-0.991	-0.938	-0.985	1.203
-0.940	-0.885	-0.947	-0.902	-0.949	-1.019	-1.052	1.165	1.089
-0.947	-0.889	-0.948	-1.015	-0.977	-1.023	1.090	1.052	1.082
-0.951	-0.917	-1.062	-1.021	-1.087	1.139	1.086	1.023	0.968
-0.980	-1.027	-1.091	-1.131	1.086	1.029	1.058	0.913	0.939
-1.094	-1.056	-1.095	1.015	0.977	1.023	0.944	0.885	0.935
-1.101	-1.170	1.057	1.012	0.949	0.910	0.942	0.881	0.928
-1.215	0.989	0.943	0.983	0.840	0.881	0.938	0.875	0.924

The estimated transformation matrix $\hat{\mathbf{M}}_{\mathrm{trans}}$ is then calculated as Eq. 4.30 and is visu-

alized by the colour map shown in Fig. 5.19.

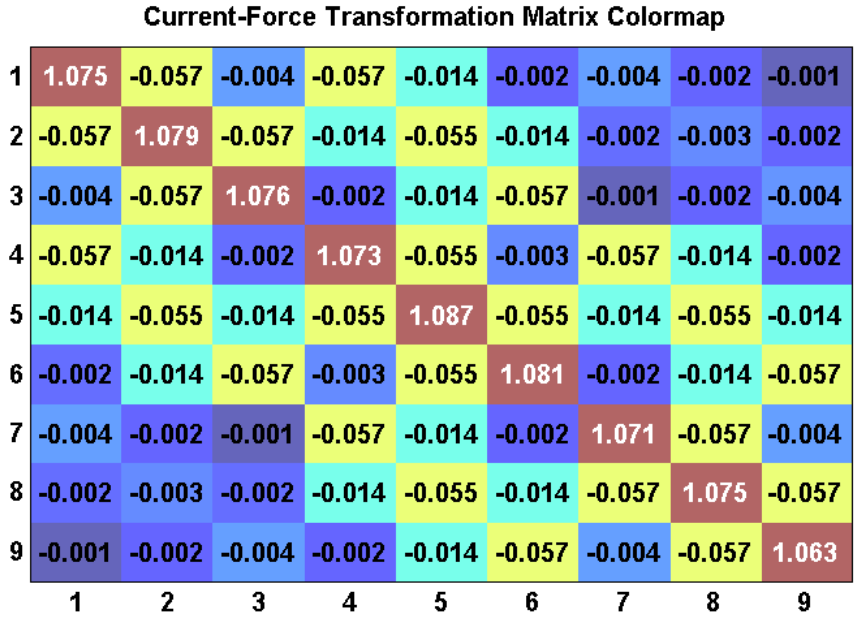

Figure 5.19: Estimated transformation matrix $\hat{\mathbf{M}}_{\text{trans}}$ for the 3-by-3 electromagnet array

It can be seen that the force on each magnet disc mainly depends on the electromagnet underneath it, while it is affected by the surrounding ones only slightly due to the designed electromagnet structure. With the estimated linear transformation $\hat{\mathbf{F}}_{\text{z}} = \hat{\mathbf{M}}_{\text{trans}}\mathbf{I}+\hat{\mathbf{b}}$, a test is then run to verify the accuracy of the transformation compared with the electromagnet array model. Using the same test cases of desired forces with that of the direct control test, the corresponding estimated current values are then calculated using

$$\hat{\mathbf{I}} = \hat{\mathbf{M}}_{\text{trans}}^{-1}(\mathbf{F}_{\text{z}} - \overline{\mathbf{F}_{\text{z}}}), \tag{5.6}$$

which results in Table. 5.6. This set of current configuration is fed into the 3-by-3 electromagnet array model to simulate the force produced using FEM. The force results are shown in Table 5.7 and are compared with the desired force values.

From the result, it can be seen that the batch model system identification reduces the MSE of the force produced by four orders of magnitude.

Table 5.6: The test case for batch model system identification of the 3-by-3 electromagnet array

Index			Force Values (N)			Current Values (A)		
1	2	3	1.00	1.90	2.00	-0.655	0.242	0.292
4	5	6	2.20	1.50	2.70	0.507	0.087	0.985
7	8	9	1.70	2.30	1.20	0.010	0.618	-0.424

Table 5.7: Test results for batch model system identification of the 3-by-3 electromagnet array

Index	Desired Force (N)	Result Force (N)	Error (N)	Mean Square Error
1	1.0	1.004	0.004	
2	1.9	1.898	0.002	
3	2.0	1.998	0.002	
4	2.2	2.202	0.002	
5	1.5	1.504	0.004	0.00001
6	2.7	2.695	0.005	
7	1.7	1.699	0.001	
8	2.3	2.302	0.002	
9	1.2	1.204	0.004	

Adaptive Control for the 3-by-3 Model

The RLS algorithm summarized in Algorithm 1 is implemented for applying the adaptive control on the 3-by-3 electromagnet array model. In the adaptive control process, for each iteration, a set of current value $\mathbf{u}(n)$ is fed into the model and the force values $\mathbf{x}(n)$ produced are extracted, the algorithm updates the estimated transformation matrix to reduce the error between the force calculated by $\hat{\mathbf{x}}(n) = \hat{\mathbf{M}}_{\text{trans}}(n)\mathbf{u}(n)$ and the force generated using FEM $\mathbf{x}(n)$. For comparison purposes, the first 10 current value sets are set as that of the test for batch model system identification listed in Table 5.3, and the desired force values for testing are the same as that of the previous two tests. To guarantee the convergence of the algorithm, the iteration number is set at 20. By using the same method to get the mean vectors as Eq. 5.5, the detrended input and state vectors can be obtained from the second iteration. The convergence on the RLS algorithm is plotted in Fig. 5.20.

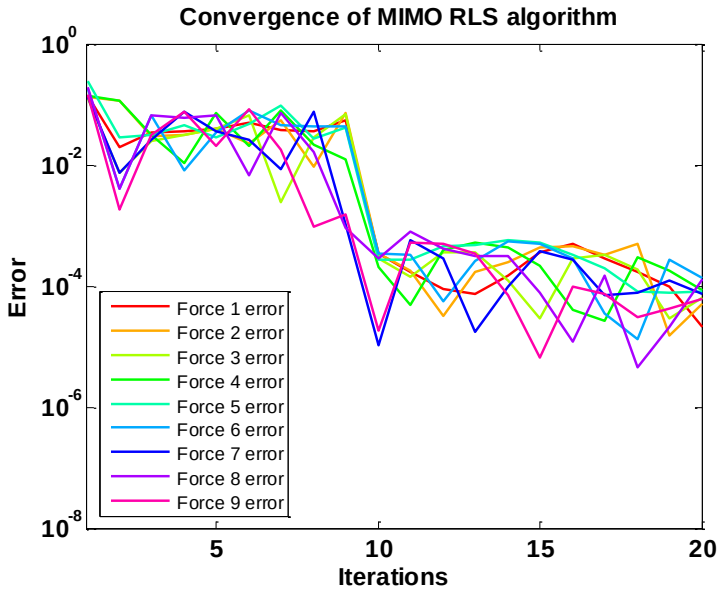

Figure 5.20: Convergence of the RLS algorithm

The horizontal axis is the iteration number, and the vertical axis indicates the error between the simulated force values and the estimated force values using the estimated transformation matrix of the current iteration. We can see from the convergence curve that the errors at the beginning are only around 0.1 owning to the good first guess, and

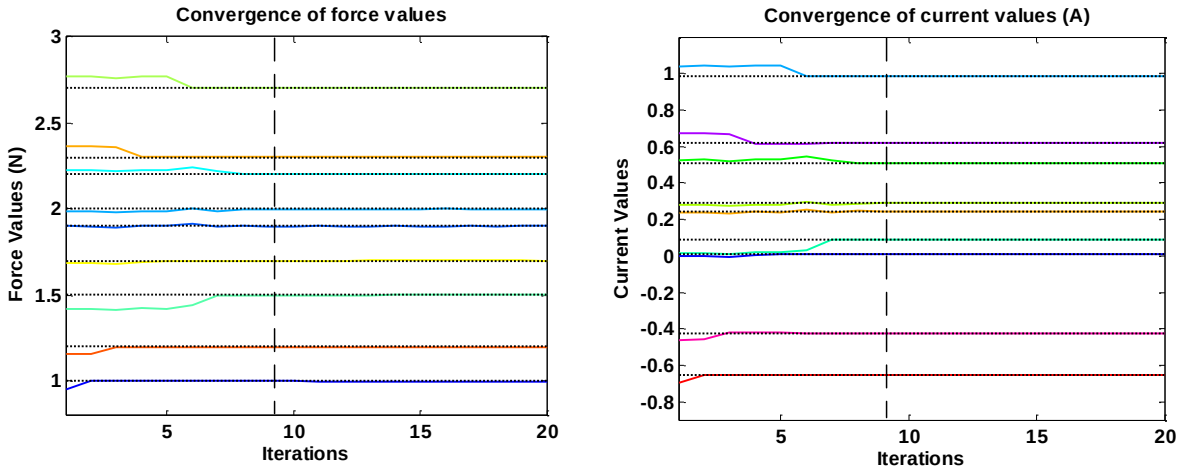

(a) Convergence of current (b) Convergence of force

Figure 5.21: Convergence analysis of the 3-by-3 array

during the first 8 iterations, the error decreases slowly with fluctuation, then it drops to 10^{-4} at the ninth iteration, and keeps going down slowly afterwards.

The effect of updating transformation matrix $\hat{\mathbf{M}}_{\text{trans}}$ can be observed in the convergence of estimated current values and the simulated force values. The estimated current values for the desired force values with the current transformation matrix are obtained and feed the estimated current values into the FEM simulation to get the resulting force at each iteration. The learning curves of the current values and force values are then depicted in Fig. 5.21a and Fig. 5.21b in comparison with Table 5.6, which are seen as the reference current configurations and force values output obtained using batch model system identification.

As can be seen in Fig. 5.21a, the current values are getting closer to the reference current configuration with each iteration, which results in Fig. 5.21b where the force values produced gradually reach the desired force values. The dashed line in both figures indicates the convergence point in consistence with the plunge in the convergence curve in Fig. 5.20.

5.4.2 Experiment on a 15-by-15 Model with 3D Human Face Surface Data

This section describes an experiment on 15-by-15 electromagnet array model aiming to produce the force field of a human face.

The adaptive control method is applied because it combines the merits of the direct control and the batch model system identification approaches. That is, the linear transformation by the estimated transformation matrix $\hat{\mathbf{M}}_{\text{trans}}$ provides a relatively low error in the beginning due to the good initialization obtained in the direct control method, and after $r = 15 \times 15 + 1 = 226$ iterations, the expected $\hat{\mathbf{M}}_{\text{trans}}$ should converge to the result in the batch model system identification approach. To verify this thought, the resulting $\hat{\mathbf{M}}_{\text{trans}}$ obtained by batch model system identification for the 15-by-15 model is used as reference.

For the RLS algorithm, 450 simulations are done with the 15-by-15 model, which is two times the theoretical number of simulations needed for convergence. The principle for selecting the current value configuration is the same as that for the 3-by-3 model, which guarantees the matrix $\mathbf{U}^T\mathbf{U}$, where $\mathbf{U}$ is the matrix formed by the first rth current value sets, is invertible. The first 226 current sets are showing in Table 5.8.

Table 5.8: First 226 current sets used in RLS for the 15-by-15 model

Simulation No.	Current Values (A)								
	I_1	I_2	I_3	I_4	...	I_{222}	I_{223}	I_{224}	I_{225}
1	-1	-1	-1	-1	...	-1	-1	-1	-1
2	1	1	1	1	...	1	1	1	1
3	-1	-1	-1	-1	...	-1	-1	-1	1
4	-1	-1	-1	-1	...	-1	-1	1	1
⋮	⋮	⋮	⋮	⋮	⋮	⋮	⋮	⋮	⋮
223	-1	-1	-1	-1	...	1	1	1	1
224	-1	-1	-1	1	...	1	1	1	1
225	-1	-1	1	1	...	1	1	1	1
226	-1	1	1	1	...	1	1	1	1

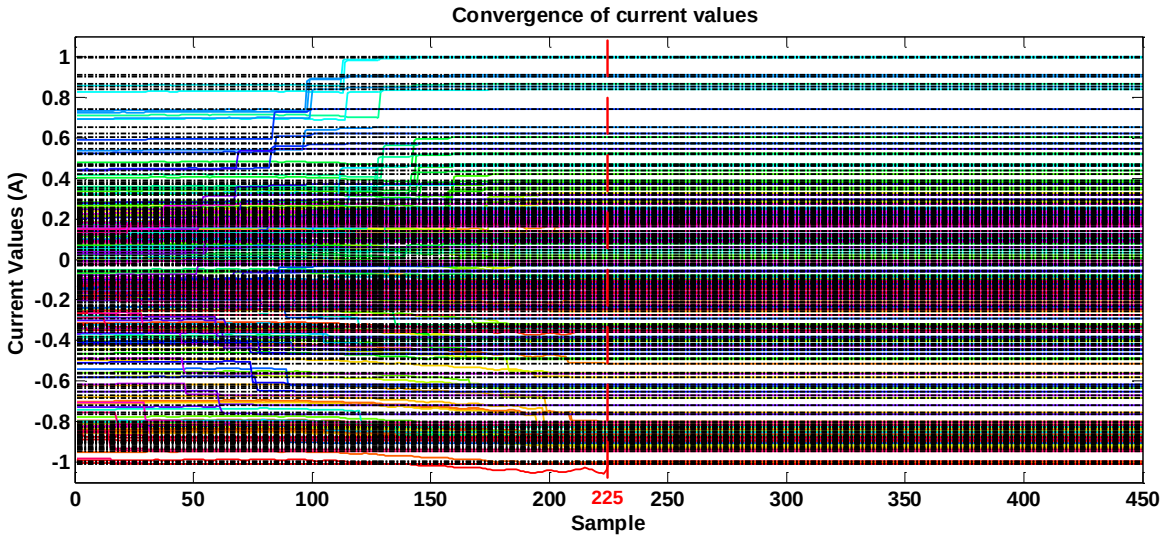

(a) Convergence of current values for the 15-by-15 model

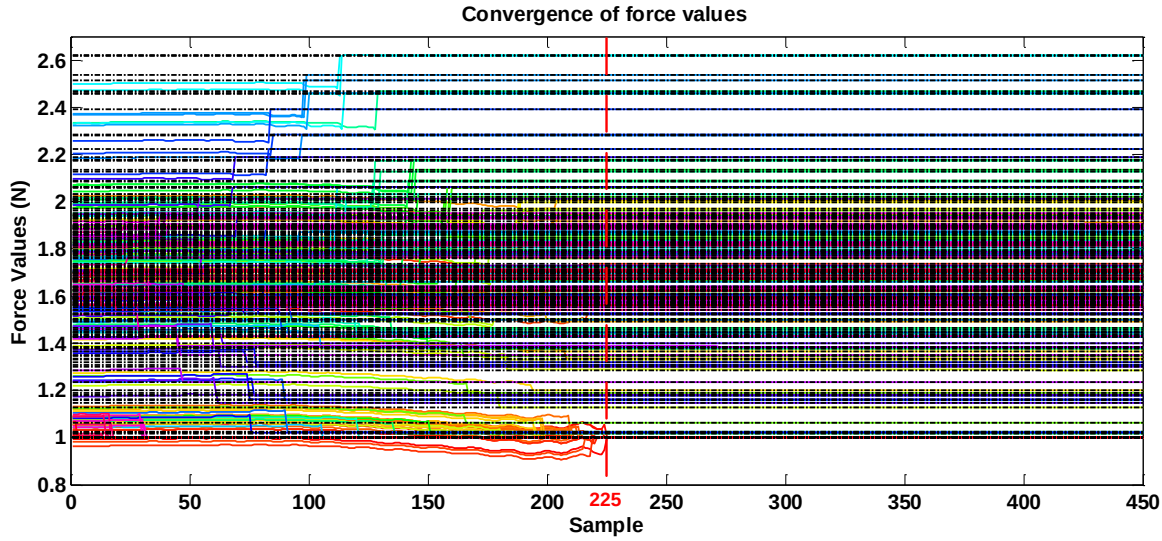

(b) Convergence of force values for the 15-by-15 model

Figure 5.22: Convergence analysis of the 15-by-15 array

The convergence of current and force values are shown in Fig. 5.22a and Fig. 5.22b, from which it can be seen that the current values converge after 225 iterations and stay stable afterwards. The transformation matrix is again calculated using Eq. 5.4.

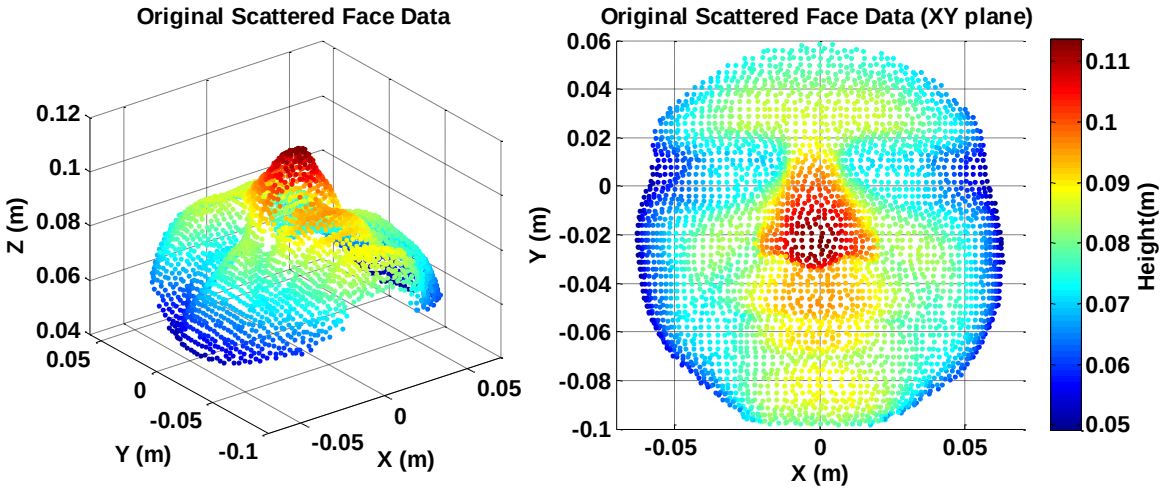

Figure 5.23: Original face surface data

The human face surface data is collected from a 3D scanner in the form of point cloud data and is saved as a PLY file. Some preprocessing techniques are applied on the data to clean it up and down-sample the large-scale data into an STL file, which can be converted into a text file for MATLAB to read in. The processed face surface data is shown in Fig. 5.23.

Because the original data set is not gridded, quantization is done first to convert the (X, Y) coordinates into a 15-by-15 gridded mesh, which results in multiple repeated data with the same (X,Y) coordinate. Removal of repeated data with the same (X,Y) coordinates is done by selecting the data with the lowest Z component, as shown in Fig. 5.24.

The Z components of the pre-processed face surface data are scaled to the range of $[0.8, 2.6]$ to fit the produced force range, and all the (X,Y) coordinates within the grid that have no data are filled with 0.8, which is the minimum force value. Thus, the desired force matrix is obtained and visualized in Fig. 5.25.

Having the desired force matrix and the estimated transformation matrix, the current configuration matrix is then obtained and is depicted using a colour map in Fig. 5.26.

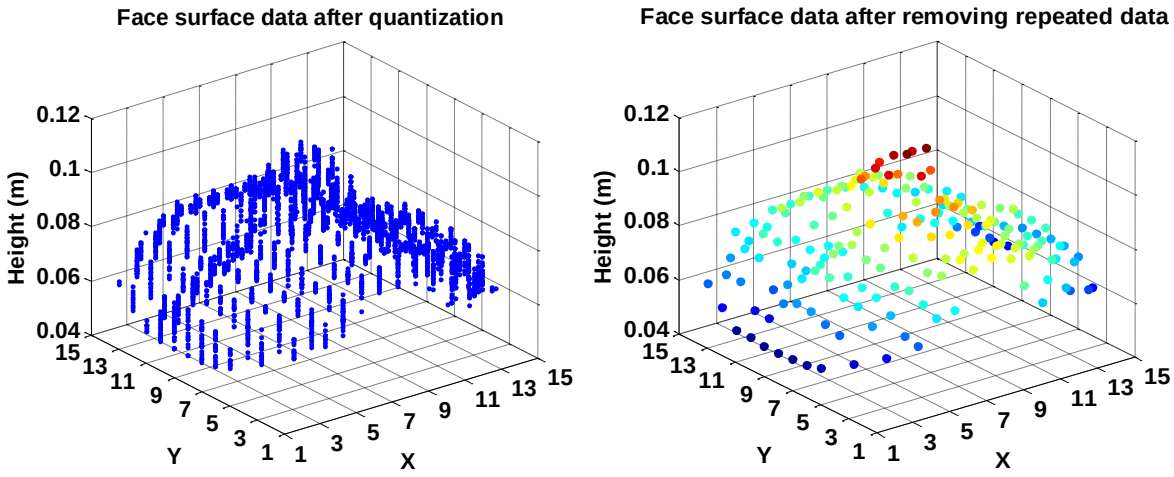

Figure 5.24: Preprocessing of the face surface data

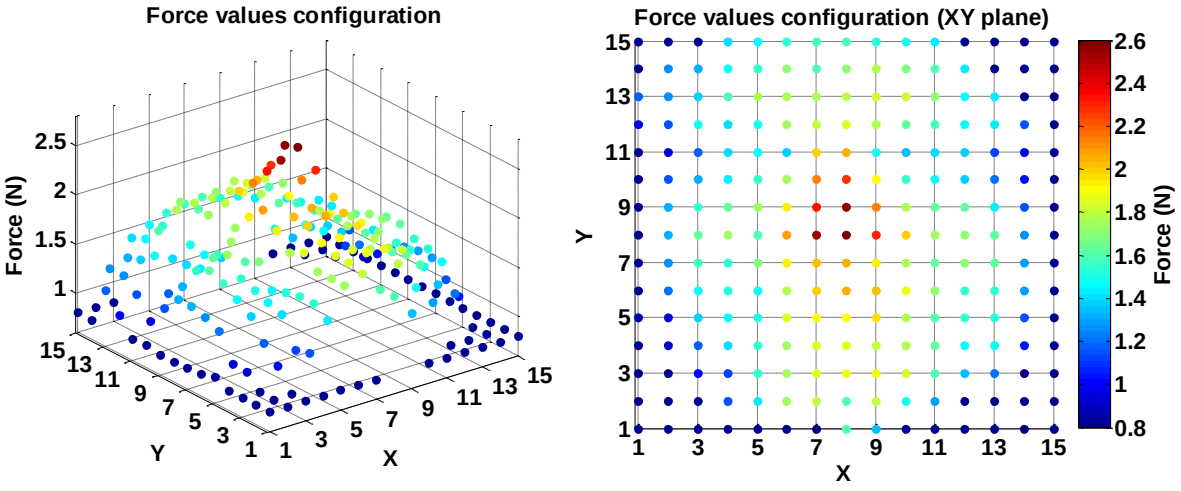

Figure 5.25: Desired force matrix for the 15-by-15 model

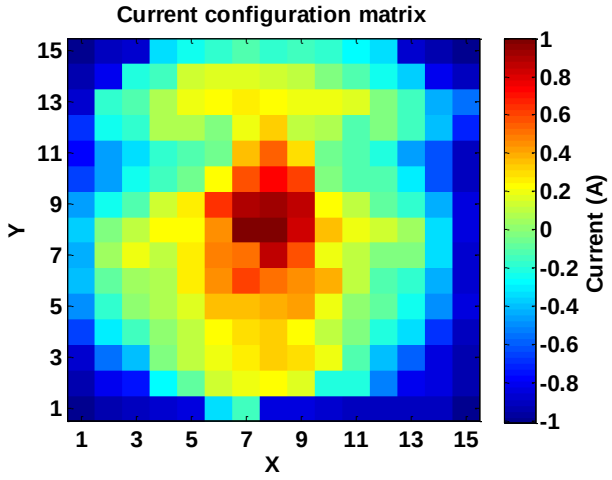

Figure 5.26: Current configuration matrix for the 15-by-15 model using volumetric face data

The MSE of the force values at the control points is 0.00001, which is negligible. The final force field generated at different distances above the array are shown in Fig. 5.27.

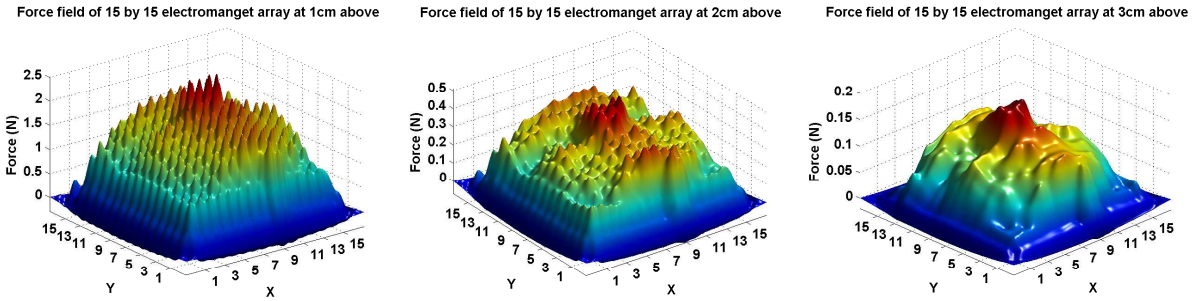

(a) Force field from 1cm above (b) Force field from 2cm above (c) Force field from 3cm above

Figure 5.27: Human face rendering test by the 15-by-15 electromagnet array

It can be seen that the force field becomes weaker but smoother as the distance increases. The force produced from 1cm above ranges from 0.8N to 2.6N; from 2cm above, it is from 0.11N to 0.49N; and from 3cm above, it is from 0.02N to 0.18N. The force field generated from 1cm is full of bumps and holes, while the fluctuation is alleviated in the force field from 2cm above, and from 3cm above the force field becomes smooth.

Chapter 6

Conclusion and Future Work

6.1 Conclusion

Mid-air haptic actuation research is of great interest for designing haptic devices that aim to produce a high fidelity haptic sensation in an intuitive way. The goal of this research is to explore the potential of controlling magnetic field for the purposes of generating tactile sensation in mid-air. In this regard, the concept of magnetic rendering is introduced, which refers to a new haptic display method applying an electromagnet array to produce magnetic field in mid-air where the force field can be felt as a magnetic repulsive force exerted on hand through the magnet discs attached.

In this research, the magnetic rendering system is proposed for rendering volumetric haptic shapes in mid-air for users to perceive with magnets attached on hands. To generate magnetic field strong enough for haptic rendering, a new electromagnet model is designed with a magnetic field concentrator and an isolator, which demonstrates desirable performance in terms of the magnitude of vertical force production, the magnetic field isolation property, and the stiffness with high fidelity via FEM simulations. The electromagnet array is configured, and its linearity is characterized, which facilitates controlling in three different approaches. FEM simulation experiments have done on a 3-by-3 model, and a 15-by-15 model with a set of pre-processed 3D scanned face data to test the force field generation performance. The direct control provides a computationally low-cost way to

generate magnetic force close to the desired values. Both the system identification and adaptive control method result in insignificant error on the control points and the RLS algorithm for adaptive control demonstrates fast convergence speed.

6.2 Future Work

To evaluate the performance of the designed magnetic rendering system, experiments have been conducted based on modelling and simulations. However, concluding remarks require a prototype of the electromagnet array to be constructed. The first prototype is on the way, which requires a significant amount of work involving testing, tuning, and real world experiments.

A foreseeable application of the designed magnetic rendering system is a 3D co-located visual and haptic display with a thin 3D hologram print placed above the electromagnet array. The 3D volumetric data will be fed both to the array and to the print, which enables the user to see the 3D object while feeling the corresponding tactile sensation.

The existing magnetic rendering system is designed for the purposes of haptic display because the control is unidirectional. In future, it is also possible to add an output feedback to the system to facilitate various applications for interaction purposes.

References

[1] R. J. Adams and B. Hannaford, "Stable haptic interaction with virtual environments," *IEEE Transactions on Robotics and Automation*, vol. 15, no. 3, pp. 465–474, 1999.

[2] M. Bergamasco, *Manipulation and Exploration of Virtual Objects*. John Wiley & Sons, 1994.

[3] M. Reiner, "The role of haptics in immersive telecommunication environments," *IEEE Transactions on Circuits and Systems for Video Technology*, vol. 14, no. 3, pp. 392–401, 2004.

[4] T. R. Coles, D. Meglan, and N. John, "The role of haptics in medical training simulators: A survey of the state of the art," *IEEE Transactions on Haptics*, vol. 4, no. 1, pp. 51–66, 2011.

[5] A. E. Saddik, "The potential of haptics technologies," *IEEE Instrumentation and Measurement Magazine*, vol. 10, no. 1, pp. 10–17, 2007.

[6] V. Hayward, O. R. Astley, M. Cruz-Hernandez, D. Grant, and G. Robles-De-La-Torre, "Haptic interfaces and devices," *Sensor Review*, vol. 24, no. 1, pp. 16–29, 2004.

[7] K. Salisbury, F. Conti, and F. Barbagli, "Haptic rendering: introductory concepts," *IEEE Transactions on Computer Graphics and Applications*, vol. 24, no. 2, pp. 24–32, 2004.

[8] G. Bianchi, B. Knoerlein, G. Szekely, and M. Harders, "High precision augmented reality haptics," in *Proceedings of EuroHaptics*, vol. 6, pp. 169–178, 2006.

[9] "Geomagic touch x." http://www.geomagic.com/en/products/phantom-desktop/overview. Accessed: 2015-01-30.

[10] P. Berkelman, "A novel coil configuration to extend the motion range of lorentz force magnetic levitation devices for haptic interaction," in *Proceedings of IEEE/RSJ International Conference on Intelligent Robots and Systems*, pp. 2107–2112, 2007.

[11] R. Traylor and H. Z. Tan, "Development of a wearable haptic display for situation awareness in altered-gravity environment: Some initial findings," in *Proceedings of the 10th IEEE Symposium on Haptic Interfaces for Virtual Environment and Teleoperator Systems*, pp. 159–164, 2002.

[12] H. Kim, C. Seo, J. Lee, J. Ryu, S. Yu, and S. Lee, "Vibrotactile display for driving safety information," in *Proceedings of IEEE Intelligent Transportation Systems Conference*, pp. 573–577, 2006.

[13] K. Minamizawa, D. Prattichizzo, and S. Tachi, "Simplified design of haptic display by extending one-point kinesthetic feedback to multipoint tactile feedback," in *Proceedings of IEEE Haptics Symposium*, pp. 257–260, 2010.

[14] D. Prattichizzo, F. Chinello, C. Pacchierotti, and M. Malvezzi, "Towards wearability in fingertip haptics: a 3-dof wearable device for cutaneous force feedback," *IEEE Transactions on Haptics*, vol. 6, no. 4, pp. 506–516, 2013.

[15] Y. Suzuki and M. Kobayashi, "Air jet driven force feedback in virtual reality," *IEEE Transactions on Computer Graphics and Applications*, vol. 25, no. 1, pp. 44–47, 2005.

[16] R. Sodhi, I. Poupyrev, M. Glisson, and A. Israr, "Aireal: interactive tactile experiences in free air," *ACM Transactions on Graphics*, vol. 32, no. 4, p. 134, 2013.

[17] S. Gupta, D. Morris, S. N. Patel, and D. Tan, "Airwave: Non-contact haptic feedback using air vortex rings," in *Proceedings of the ACM International Joint Conference on Pervasive and Ubiquitous Computing*, pp. 419–428, 2013.

[18] T. Hoshi, M. Takahashi, T. Iwamoto, and H. Shinoda, "Noncontact tactile display based on radiation pressure of airborne ultrasound," *IEEE Transactions on Haptics*, vol. 3, no. 3, pp. 155–165, 2010.

[19] B. Long, S. A. Seah, T. Carter, and S. Subramanian, "Rendering volumetric haptic shapes in mid-air using ultrasound," *ACM Transactions on Graphics*, vol. 33, no. 6, p. 181, 2014.

[20] M. Weiss, C. Wacharamanotham, S. Voelker, and J. Borchers, "Fingerflux: near-surface haptic feedback on tabletops," in *Proceedings of the 24th ACM Annual Symposium on User Interface Software and Technology*, pp. 615–620, 2011.

[21] P. Berkelman, M. Miyasaka, and J. Anderson, "Co-located 3D graphic and haptic display using electromagnetic levitation," in *Proceedings of IEEE Haptics Symposium*, pp. 77–81, 2012.

[22] H. E. Knoepfel, *Magnetic Fields: A Comprehensive Theoretical Treatise for Practical Use*. John Wiley & Sons, 2008.

[23] J. Jansen, C. Van Lierop, E. Lomonova, and A. Vandenput, "Modeling of magnetically levitated planar actuators with moving magnets," *IEEE Transactions on Magnetics*, vol. 43, no. 1, pp. 15–25, 2007.

[24] J. Compter, "A planar motor with electrodynamic propulsion and levitation under 6-DoF control," in *Proceedings of the 4th International Symposium on linear Drives for Industry Applications*, 2003.

[25] J. C. Mallinson, "One-sided fluxes–a magnetic curiosity?," *IEEE Transactions on Magnetics*, vol. 9, no. 4, pp. 678–682, 1973.

[26] P. Sankar, "Magnetic arrays with increased magnetic flux," Aug. 20 2013. US Patent 8,514,047.

[27] S. Vonsovskii, *Magnetizm (Magnetism)*. Moscow: Nauka, 1971.

[28] S. Sanz, L. Garcia-Tabares, I. Moya, D. Obradors, and F. Toral, "Evaluation of magnetic forces in permanent magnets," *IEEE Transactions on Applied Superconductivity*, vol. 20, no. 3, pp. 846–850, 2010.

[29] H. Cramér, *Mathematical Methods of Statistics*, vol. 9. Princeton university press, 1999.

[30] J. Elkind, D. Green, and E. Starr, "Application of multiple regression analysis to identification of time-varying linear dynamic systems," *IEEE Transactions on Automatic Control*, vol. 8, no. 2, pp. 163–166, 1963.

[31] P. Eykhoff, "Process parameter and state estimation," *Automatica*, vol. 4, no. 4, pp. 205–233, 1968.

[32] D. Kleinbaum, L. Kupper, A. Nizam, and E. Rosenberg, *Applied Regression Analysis and Other Multivariable Methods*. Cengage Learning, 2013.

[33] M. Athans, "The matrix minimum principle," *Information and control*, vol. 11, no. 5, pp. 592–606, 1967.

[34] M. H. Hayes, *Statistical Digital Signal Processing and Modeling*. John Wiley & Sons, 2009.

[35] B. Widrow and S. D. Stearns, *Adaptive Signal Processing*, vol. 1. Englewood Cliffs, NJ, Prentice-Hall Inc., 1985.

[36] W. Liu, J. C. Principe, and S. Haykin, *Kernel Adaptive Filtering: A Comprehensive Introduction*, vol. 57. John Wiley & Sons, 2011.

[37] S. Haykin and B. Widrow, *Least-mean-square Adaptive Filters*, vol. 31. John Wiley & Sons, 2003.

[38] S. S. Haykin, *Adaptive Filter Theory*. Pearson Education India, 2007.

[39] M. Krein, "Integral equations on a half-line with kernel depending upon the difference of the arguments," *American Mathematical Society Translations Series 2*, vol. 22, pp. 163–288, 1962.

[40] D. Wiberg, "Dynamic system identification: Experiment design and data analysis," *IEEE Transactions on Automatic Control*, vol. 28, no. 10, pp. 999–1000, 1983.

[41] APW Company, "Electromagnets and custom electrical coils." http://catalog.apwcompany.com/viewitems/all-categories/ellaneous-products-and-assemblies-electrical-coils?&bc=100&gclid=CIfkvtW13r4CFeY-Mgod7CwA0g. Accessed: 2015-02-02.

[42] A. S. B258-02, "Standard specification for standard nominal diameters and cross-sectional areas of awg sizes of solid round wires used as electrical conductors," 2008.

[43] Magnetic Shield Corporation, "Mumetal stress annealed sheet." http://custommagneticshielding.magneticshield.com/viewitems/mumetal-sheet-and-foil/mumetal-stress-annealed-sheet?&sortid=1032&measuresortid=256&sortorder=desc&pagesize=50. Accessed: 2015-02-05.

[44] A. S. Householder, *The Theory of Matrices in Numerical Analysis*. Blaisdell, New York, 1964.

[45] COMSOL Multiphysics, "Introduction to comsol multiphysics." http://www.comsol.no/shared/downloads/IntroductionToCOMSOLMultiphysics.pdf. Accessed: 2015-01-05.

[46] C. Multiphysics, "Livelink for matlab," *Users guide, Version 4*.

[47] G. C. Burdea, G. C. Burdea, and C. Burdea, *Force and Touch Feedback for Virtual Reality*. Wiley New York, 1996.

[48] K. J. Kuchenbecker, J. Fiene, and G. Niemeyer, "Improving contact realism through event-based haptic feedback," *IEEE Transactions on Visualization and Computer Graphics*, vol. 12, no. 2, pp. 219–230, 2006.